August 2020

Pattern Formation and Elastocapillary Instabilities in Soft Gels

Xingchen Shao
Clemson University, xingchs@g.clemson.edu

Pattern formation and elastocapillary instabilities in soft gels

---

A Dissertation
Presented to
the Graduate School of
Clemson University

In Partial Fulfillment
of the Requirements for the Degree
Doctor of Philosophy
Mechanical Engineering

---

by
Xingchen Shao
August 2020

Accepted by:
Dr. Joshua Bostwick, Committee Chair
Dr. John R. Saylor, Committee Co-Chair
Dr. Nicole Coutris
Dr. Phanindra Tallapragada

Abstract

Hydrogels are complex materials that are typically utilized as bioinks in the emerging 3D bioprinting technology. Gels are distinguished by an elasticity that introduces complexity into the pinch-off process. The distinguishing feature of soft gels is that capillarity (surface tension) and elasticity are comparable which can induce an abundance of new phenomena in the elastocapillary regime. Unfortunately, elastocapillary instabilities are not fully understood because classical theories of fluid mechanics and solid mechanics can not capture the crossover between capillary-dominated and elasticity-dominated dynamics. Herein, elastocapillary surface phenomena on hydrogels are experimentally characterized and new theoretical models are proposed to interpret the discrepancies between classical theories and new experimental observations. Many first observations of dynamic elastocapillary phenomena are reported including the experimental observations of i) gel drop oscillations in ultrasonic levitation and ii) Faraday waves on mechanically-vibrated gels. The mechanism of pattern formation is investigated and the role of elasticity is revealed. By relating theory to experiment, a new diagnostic technique to measure the surface tension and rheology of soft gels is developed, which can directly support many emerging 3D bioprinting technologies.

Acknowledgments

I remember the first day I knocked Dr. Bostwick's door asking whether a Ph.D position was available in his group. At that time, I knew nothing about doing research, I did not speak English well and even did not understood what he was talking about, but I still claimed myself was very motivated by his study. This was the beginning of my journey in Clemson. When I recall this now, I have to acknowledge that I was very lucky! In our first formal meeting, Dr. Bostwick introduced Dr. Saylor to me who has played a crucial role for my success in this Ph.D journey. Dr. Bostwick and Dr. Saylor, they are two giants inspire me to move forward, encourage me to be stronger, and support me when I am in hard days.

I would like to thank Drs. Delhaye and Coutris for always taking care of my study and giving me lots of useful suggestions. I would express my special thanks to Dr. Coutris. Without her recommendation, I would not have known Dr. Bostwick. I would also like to thank Dr. Tallapragada for serving on my dissertation committee and giving me feedback on my work.

I would like to thank all my lab mates for lots of interesting discussions and trouble shooting.

Lastly, I would like to thank my parents Caiwei Shao and Lindi Shan. They are always very proud of me and support me to pursue what I think I should.

Contents

List of Tables

List of Figures

Chapter 1

Introduction

Capillary instabilities have been a historically significant problem in modern physics and have aroused a wide range of interests for several generations, primary because relatively simple fluidic systems can induce intrinsically nonlinear spatial and temporal patterns [49, 32]. Generally, capillary forces control the dynamics of a fluid system when the characteristic length l is smaller than the capillary length scale $l_c = \sqrt{\sigma/g\rho}$ where σ is the surface tension of the fluids, ρ is the density of the liquid, and g is the gravitational acceleration. When instability occurs, the reconfiguration dynamics occur on time scales associated with the capillary time $t_c = \sqrt{\rho l^3/\sigma}$. The most easily observed capillary phenomenon are gravity-capillary surface waves, which follow the dispersion relationship

$$\omega = \sqrt{gk + \frac{\sigma}{\rho}k^3}, \tag{1.1}$$

where k is the continuous wavenumber. Surface tension effects dominate for small wavelengths $\lambda \sim 1/k \ll l_c$ and gravitational effects for long wavelengths $\lambda \gg l_c$. Surface waves can also occur on an inviscid liquid drop and induce shape oscillations when an integer number of wavenumbers exist on the drop. The resonance frequency prediction for the shape oscillation on an inviscid liquid drop was given by Lord Rayleigh

$$f = \frac{1}{2\pi}\sqrt{\frac{\sigma n(n-1)(n+2)}{\rho R^3}}, \tag{1.2}$$

where n represents the discrete oscillation mode number and R is the equilibrium drop radius [129]. In both of these cases, surface tension resists deformation and is a stabilizing force. Surface tension can also drive instability, as with the Plateau-Rayleigh instability describing the breakup of a liquid

column into drops to minimize surface area [125, 129]. Gravitational force can similarily drive instability resulting in the finger-like patterns between two fluids of different densities when the gravitational acceleration is directed into the lighter one, as in the Rayleigh Taylor Instability[85]. Interfacial instability can also occur in systems driven by periodic forcing. Faraday waves can be excited on the free surface of liquid when the vertical excitation amplitude exceeds a threshold[42] and theses are synonymous with pattern selection phenomena and can exhibit hexagons, squares or stripe symmetry, to name a few[76, 75, 14].

The aforementioned are all canonoical hydrodynamic instablities and extensions have been made in the literature to account for liquid viscosity, wetting, and nonlinear effects. Capillary-gravity waves constrained with different wetting boundaries, e.g., free-end edge and pinned-end edge can exhibit frequency shifts and damping due to dynamic wetting effects even for inviscid liquids [135, 56]. Material properties can affect mode selection and change the thresholds of Faraday waves patterns [76, 43] and nonlinear analysis is used to study the pattern formation on Faraday waves [163]. For example, thin viscous films subject to vertical vibration have been shown to exhibit a harmonic response as opposed to the classic subhamonic response of Faraday waves and this is attributed to the strong viscous effects for this system [112]. Notably, sessile drop oscillations can be viewed as an extension to Rayleigh drops but with wetting effects and it has been recently shown that the oscillation spectrum fills a droplet motion periodic table [140, 28].

Research into capillary phenomena has moved many industrial process forward, as the study of droplet oscillation facilitates numerous technologies, such as atomization [127], pulmonary drug delivery[166], aerosol scavenging[46], and inkjet printing [24], to name a few. The dynamics in the Rayleigh-Taylor instability is similar to some mixing processes in atmospheric flows resulting from varible density[84] and it is reponsible for nuclear bubbles formed in central heavy-ion collisions[109]. Viscous effects in Plateau-Rayleigh breakup aid in delaying the onset of instability and plays an important role in precision inkjet processes [19, 65]. Capillary-gravity waves can enhance the mass and heat transfer across the gas-liquid interface[158, 121], and the formation of which is crucial in oceangraphy to understand the process of wind energy inputting through the ocean surface [4, 161]. The dispersion relationship of capillary-gravity waves is utilized to develop some non-contacting detection techniques for different purposes[59, 100]. This approach has been extended to the rheological measurements in viscoelastic materials and shows advantage over traditional measurement methods[138, 137, 26].

The goal of this thesis research is to investigate capillary instabilities in soft gels. It is hopeful that the fundamental questions addressed in this dissertation will influence the emerging field of elastocapillarity and associated industrial processes in the same manner as the aforementioned canonical hydrodynamic instabilities have done.

1.1 Motivation of this dissertation

The motivation of this dissertation comes from recent developments in biomaterials and bioprinting technology [115], which has been applied to wound regeneration and has the potential to build human organs and viable tissue. A bioprinting device is a computer-assisted process to accurately deliver bioink drops which are typically cell-laden hydrogels to create complex 3D biostructures [44, 160]. The bioinks pinch off into drops from the printer nozzle with appropriate size and speed and are deposited in a desired pattern. The physical process is similar to traditional inkjet printing with the exception that hydrogels are capable of sustaining biological functions and are characterized by complex rheological properties, including both viscosity and finite elasticity [13, 51]. In spite of tremendous advancement, bio-printing technology often suffers from low resolution of the printed structures. For example, uncontrollable instability happens when the bioink is extruded through the nozzle that compromises the geometrical fidelity of bio-printed constructs and the unpredictable pinch off drop sizes can cause damage to the cell encapsulated [40]. The reason for the unstable printing process lies in the existence of an elasticity in the printing materials that makes the dynamics more challenging to control than pure liquids, and which is an obstacle to design a more precise and reliable 3D bio-printer.

Bioinks are complex materials and there are generally two methods to study the dynamics on a viscoelastic medium with finite capillarity. The first is to treat the soft materials from a fluid mechanical perspective and incorporate the shear modulus as the imaginary part of the viscosity[52]. The other method is an elasticity based approach where the viscosity is added as the imaginary part of the shear modulus. Surface tension is related to Young-Laplace's law and is incorporated into the boundary at the interface[113, 118]. Unfortunately, none of the existing theories are capable of integrating the dynamics of fluids with a finite bulk elasticity. Onodera and Choi developed a model based on isotropic materials with elasticity and surface tension effects to study the dispersion

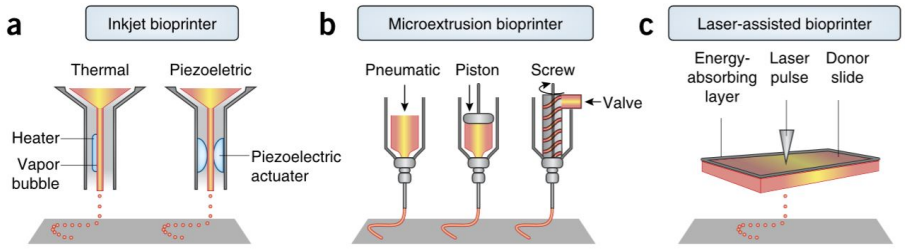

Figure 1.1: Schematic of three types of bio-printers (a) inkjet, (b) microextrusion, (c) laser-assisted. The bioinks pinch off into drops from nozzle onto a collector substrate. The pinch off process is crucial to the printing accuracy [114].

of capillary and elastic wave on the surface of soft gels, but they neglected viscous effects in their model [118]. Chakrabarti et al [26] characterized the elastocapillary effect on a soft gel slab by scaling analysis and developed an empirical model to predict the spheroidal mode ($n = 2$) of a sessile gel drop [27]. A recent theoretical model is developed to predict the elasto-capillary dispersion relationship of an elastic gel drop whose interface is held by capillary force[146].

For these reasons, systematical analysis are required to fully interpret these instability phenomenon on soft materials. This is the main motivation for this dissertation.

1.2 Definition of soft solids

The material properties of bioinks play an essential role in bio-prinitng technology. Hydrogels such as alginate, hyaluronic acid and agarose have become attractive candidates to bioinks owing to their crosslinking mechanical properties are capable of supporting appropriate cellular activity, rapid gelation process, highly biocompatibility and biodegradability over the long term [40]. In this dissertation, the focus is on instabilities and pattern formations on agarose gels, which is a sub-class of complex fluids defined by the complex modulus $G = G' + iG''$ where G' is the storage modulus and G'' is the loss modulus. The storage modulus G' measures the energy stored in the material, representing the elastic part, and the loss modulus measures the energy dissipated in the material, representing the viscous part. The loss modulus G'' and storage modulus G' are related by

$$\tan\delta = \frac{G''}{G'}, \tag{1.3}$$

where $\tan\delta$ defines the damping of the material. The storage modulus G' of gels has a constant value and is typically one order of magnitude higher than the G'' over a wide range of oscillation testing frequencies[151, 107]. Figure 1.2 is a plot of the oscillatory rheology measurements results of a typical agarose gel used in this dissertation. The results enable us to simplify the agarose gels

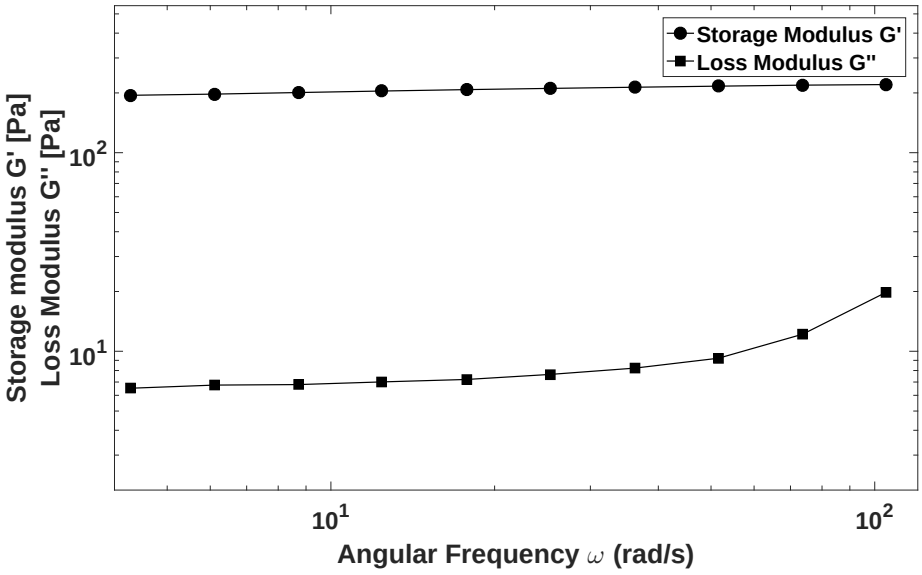

Figure 1.2: Rheology measurements of a typical agarose gel with shear modulus $G = 204.4$ Pa. The storage modulus G' is one order of magnitude higher than the loss modulus G'' over a range of oscillation testing frequencies $\omega = 4 - 105$ rad/s.

as inviscid elastic fluids with constant shear modulus $G = G'$ and negligible G'' for the range of frequencies explored here.

In general, a complex fluid possesses both a viscosity and elasticity and it is worthwhile to analyze the problem using dimensional analysis to determine the dominate balance of forces controlling the dynamics. For fluids with a free surface, the capillary force dominates flows and the dynamics are characterized by three time scales; relaxation time $t_p = \tau$ which describes the time scale needed for the material to reach equilibrium stress state after it has been deformed, a viscous time scale $t_v = \mu l/\sigma$ with μ the viscosity, and an inertial time scale $t_c = \sqrt{\rho l^3/\sigma}$. Two dimensionless numbers are defined by characterizing the relative balances of these three time scales: the Deborah number $De \equiv t_p/t_c = \tau/\sqrt{\rho l^3/\sigma}$, which represents the elasticity of materials; the Ohnesorge number $Oh \equiv t_v/t_c = \mu/\sqrt{\rho l^3/\sigma}$, which balances the viscosity to the materials inertial and surface tension.

For the special case of inviscid elastic fluids, the three time scales are ordered as $t_p > t_c > t_v$, which corresponds to $De > 1 > Oh$. The agarose gels studied in this dissertation belong to this category of inviscid elastic materials with finite surface tension.

One novel and distinguishing feature of soft gels is that capillarity can dominate the dynamic response [144, 2]. Some preliminary experiments have highlighted the surface tension effect in the smoothing of features on soft solids which is known as elastocapillarity. This is readily seen in a soft rod with asymmetic cross section that can be bent significantly by surface tension[106], the wetting of droplets on soft substrates that can deform the three phase contact-lines[86, 142], and the flattening of the corner of a soft gel after being released from a square pattern mold[119]. The physics behind these results can be understood by considering the relative balance between the elasticity and surface tension, which is defined as the elastocapillary length $L_e = \sigma/E$. Consider an elastic solid with E as the shear modulus and mean curvature K, under a strain ϵ, the elastic force is balanced by the capillary force so that $\sigma K \sim \epsilon E$. For significant deformations, $1/K \sim \epsilon E$, which suggests the capillary effect becomes important when the geometric length $1/K$ is smaller than L_e[144]. The elastocapillary length for common materials is smaller than the atomic scale and this is the reason the surface tension effects on most materials like metal and glass are negligible. But the elastocapilary length on a typical agarose gel (E=30Pa) can be millimeter sized, which means the role of capillarity is observable when the geometrical length is also on the order of millimeters. Alternatively, surface tension can deform thin sheets with large shear modulus when $1/K \ll \epsilon E$. For example, a slender elastic structure with thickness b is deformed by a liquid droplet of characteristic length R[126, 131]. To avoid confusion with elastocapillarity, this new phenomenon refers to bendocapillarity, which corresponds to a new length scale $L_b = \sqrt{Eb^3/\sigma}$ [144].

Some canonical capillary phenomenon on liquids have been observed on soft solids, and it is perhaps unsurprising that theories based solely on either fluid mechanics or solid mechanics can break down in the elastocapillary regime. Mora *et al.* observed Plateau-Rayleigh Instability (PRI) on soft gels and a dimensionless elastogravity number which relates the elastocapillary length with the material density is put forward to predict the thresholds of PRI on soft solids [107]. Rayleigh-Taylor instabilities were reported on a soft gel whose interface facing downwards is consistent with the required adverse density gradient[108]. Monroy and Langevin observed elastocapillary dispersion relationship for surface waves on gels, which covers the crossover for the capillary waves to elastic waves [104]. Their results indicate the classic Rayleigh elastic waves theory which can successfully

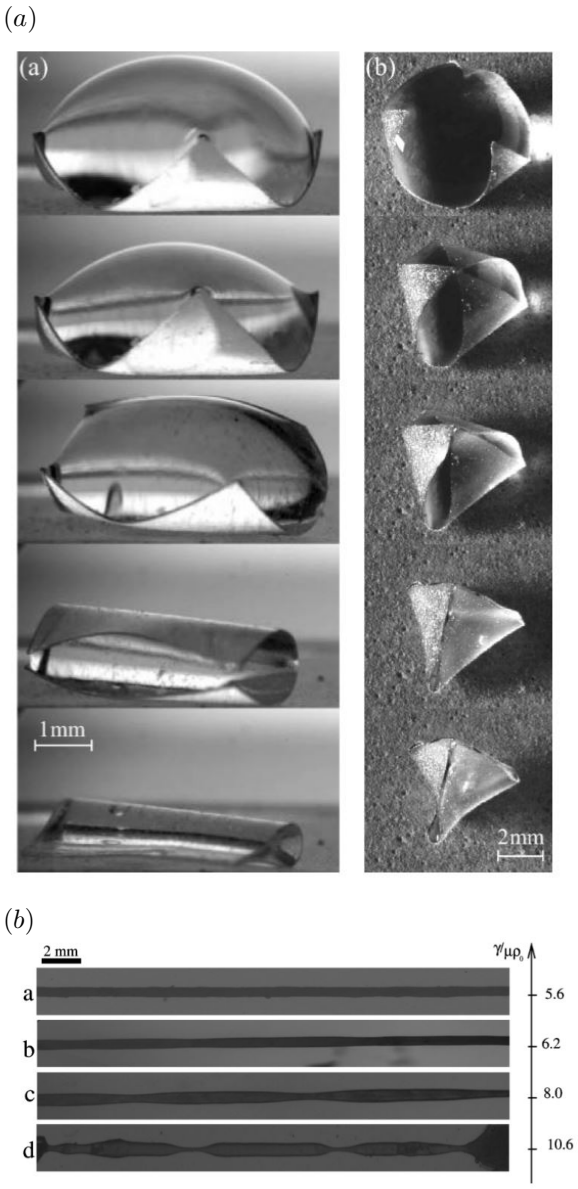

Figure 1.3: (*a*) Examples of bendocapillarity [126]. Elastic sheets are deformed by surface tension of a liquid droplet and the evaporation of the droplet manipulates a self-folding effect to the capillary origami sheet. (*b*) Example of elastocapillarity [107]. Plateau-Rayleigh instability is observed on a soft gel rod when the elastic energy of the gel is comparable to surface energy.

predict non-dispersive surface waves on solids is not applicable when the material is in the elastocapillary regime. Chakrabarti and Chaudhury reported elastocapillary dispersion relationships in a vibrational sessile gel drop [26], which is beyond the prediction of the purely elastic theory of a solid drop oscillation. The classic Young's equation for wetting can no longer predict the droplet contact angle on a soft solid substrate, because the droplet surface tension can deform soft solid substrates[91, 61]. Similarly, the Johnson-Kendall-Roberts theory which is the basis of modern contact mechanics breaks down on very soft solids, which is a consequence of neglecting the role of surface tension [143]. Soft solid composites are stiffened by spherical liquid droplet inclusions when the elastocapillary number $\sigma/RE \gg 1$, which contradicts the classic Eshelby theory in composite mechanics [141]. These discrepancies between theories of classical mechanics and experimental observations on soft solids motivate further investigation into dynamic elastocapillary effects in new experiments and the corresponding development of new theories to interpret those observations. This is the focus of this dissertation.

1.3 Summary of this dissertation

In this dissertation, elastocapillary instabilities on soft gels are studied from both the experimental and theoretical perspective for four physical systems. Several fundamental elastocapillary instabilities are discovered and the corresponding theoretical models are developed to predict these newly discovered phenomenon. The main contributions include:

1. The experimental observation of the crossover between capillary-dominated and elastic-dominated planar waves over a large range of shear modulus, which agrees favorably with an asymptotic closed-form dispersion relationship.

2. The first experimental observation of shape mode oscillations in a gel drop using ultrasonic levitation. A technique is then developed to measure the rheological properties of soft gels using the frequency response of droplet oscillations.

3. Experimentally quantification of the effects of viscosity, shear modulus, and surface tension on the frequency response of harmonically-excited axisymmetric edge waves.

4. The first experimental observation of Faraday waves on soft gels and cataloging of a large number of surface modes.

Chapter 2

Extracting surface tension on soft gels from mechanically-excited planar surface waves

Reproduced from [Shao X, Saylor JR, Bostwick JB. Extracting the surface tension of soft gels from elastocapillary wave behavior. Soft matter. 2018;14(36):7347-53] with permission from the Royal Society of Chemistry.

2.1 Introduction

Capillary instabilities in Newtonian fluids are widely used in industrial processes such as spray cooling, inkjet printing/rapid prototyping, turbulent mixing, and the float-zone method of crystal growth. Recent interest in bio-printing technologies such as cell printing and tissue engineering use these basic principles but adapted to bioinks [67, 145], which are typically hydrogels with complex rheologies characterized by non-trivial elasticity that are capable of sustaining biological function. In this paper, the experimental observation of parametrically-excited surface waves on soft agarose gels is reported and the dispersion relationship over a large range of shear modulus is characterized. A new technique is presented for measuring the surface tension of soft hydrogels.

Traditional surface tension measurement techniques, such as the Du Nüoy tensiometer or

Wilhelmy plate, work well for liquid interfaces but are difficult to apply to soft hydrogels. Alternative methods measure the solid surface tension as a fitting parameter that characterizes an observed property of the interface, such as the geometry the wetting ridge [142], the shape of the solid meniscus during indentation [165, 164], or the statistical distribution of delay times during fracture nucleation [50]. Notably, a bridge tensiometer has recently been used to measure the surface tension of yield stress materials, such as Carbonpol gel. Specifically, the surface tension is extracted from an elastoplastic model that delineates elastic from yield stress effects[68]. Here a technique which uses the dispersion relationship of mechanically-excited surface waves to measure the solid surface tension of soft gels is established. The technique is distinguished by its simplicity, as the experiments use equipment that is both common and inexpensive.

Recent work has shown that surface tension forces can dominate the dynamics of soft gels, leading to Rayleigh-Taylor [108] and Plateau-Rayleigh [106] instabilities. Capillary-gravity waves travel on a liquid/gas interface endowed with surface tension [128, 79] and obey the dispersion relationship

$$\omega = \sqrt{gk + \frac{\sigma}{\rho}k^3}, \tag{2.1}$$

where ω is the angular frequency, k is the wavenumber, g is the gravitational constant, σ is the liquid/gas surface tension, and ρ is the liquid density. Capillary-gravity waves have been well-studied because they are relevant to numerous technologies that occur over many length scales; e.g. gravity waves are responsible for momentum exchange between atmospheric layers [47], whereas capillary waves are utilized in pulmonary drug delivery systems such as nebulizers [139] and are prevalent in wave dissipation (breaking) [99] and gas/momentum exchange [98, 34, 132, 133] in oceanography.

In contrast to capillary-gravity waves, Rayleigh surface waves on linear elastic solids are non-dispersive or have constant wave speed [130]. The dispersion relationship is given by

$$\omega = C\sqrt{\frac{G}{\rho}}k \tag{2.2}$$

where G is the shear modulus, and can be used to measure shear elasticity in solids [21, 168]. The constant C encompasses properties such as material compressibility and finite-depth effects. For reference, $C = 0.955$ for incompressible materials of semi-infinite extent. The non-dispersive nature of Rayleigh waves is used in non-destructive material testing to identify cracks [80, 94], geotechnical

analysis of underwater [87] and subsurface [120] features, and the food science industry for quality control and sorting [62, 55], and in magnetic resonance elastography (MRE) [116, 90].

Waves on soft materials are known to possess properties of both capillary and elastic waves. The crossover from capillary to elastic waves has been experimentally observed in electrically-excited traveling waves on agarose gels [104, 30, 29], and in ultrasonically-excited soft viscoelastic layers [149]. Observations, in general, match a predicted dispersion relationship derived from either an elastic [118] or fluid [52] based model, both of which include elastic and surface tension effects. More complex models for capillary waves that account for viscoelastic substrate effects have also been put forth [54, 117, 70]. A historical perspective is given in the recent article by Monroy[103]. For ultra-soft solids, the self-weight of the gel can become important as seen in gravity-driven instabilities [108] and the results reported here.

Herein Faraday waves are used to investigate the dispersion relationship of soft hydrogels and to study the transition from capillary to elastic waves. Faraday waves are formed at an interface by a parametric instability when the system is vibrated in the vertical direction, resulting in a wave having a frequency half that of the forcing frequency[41]. For Newtonian fluids, the literature on Faraday waves is vast (see review in Miles & Henderson[101]), whereas that for viscoelastic liquids is comparatively small [110, 159, 7, 22, 6]. Notably, Kumar[78] studied this system analytically, exploring the relative strengths of elastic and viscous forces on the onset amplitude and showing the existence of harmonic forcing (not the expected subharmonic) when the elastic forces are strong. However, to the best of our knowledge, Faraday waves have not been used as a means to investigate the dispersion relationship for soft hydrogels.

This project develop an experimental protocol for exciting and characterizing surface waves on soft agarose gels with shear modulii ranging from $G = 1\text{Pa}$–260Pa. The experiments yield a dispersion relationship for each shear modulus from which the transition from capillarity-dominated to elasticity-dominated dynamics is captured. A theoretical dispersion relationship is developed and a method of extracting the solid surface tension [66, 142, 15] is shown from the experimental data. This new technique is a relatively simple way to measure the surface tension of soft hydrogels. It is concluded by discussing the relevance of the experimental technique and analysis to technologies that concern the dynamics of soft hydrogels.

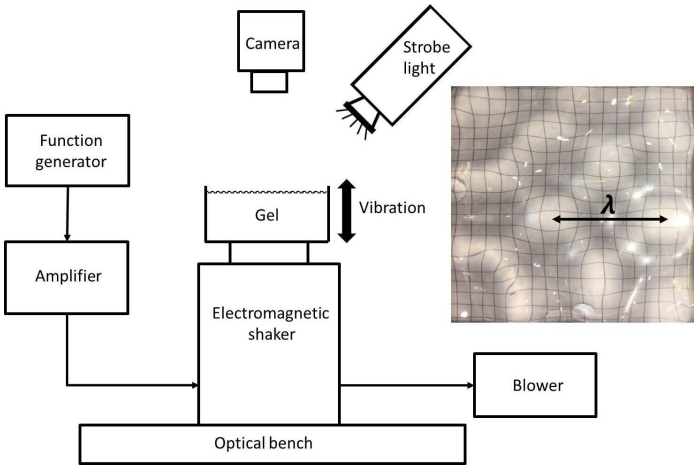

Figure 2.1: Schematic of the experimental apparatus with typical surface wave image with wavelength λ.

2.2 Experimental procedure

Faraday waves are investigated on soft agarose gels using the experimental setup shown in Figure 2.1. A 9 cm $\times$9.5 cm plexiglass container filled with agarose gel is vertically driven by a shaker over a range of driving frequencies $f_d = 60 - 200$Hz. The shaker is driven by a function generator/amplifier combination. Surface instabilities with square wave symmetry, shown in Figure 2.1, were observed above a threshold forcing amplitude. Images are captured using a strobe light and digital camera mounted above the container.

The hydrogels are prepared by dissolving agarose powder (Sigma Aldrich Type VI-A) in deionized water using the method of [151]; the liquid mixture is kept at 90°C for 1 hour before being cast into the container and allowed to cool at room temperature overnight. A gel height $h = 24$mm is chosen to minimize finite-size depth effects, such that the solid can be treated as semi-infinite. The concentrations are investigated in the range $\phi = 0.06 - 0.275$%w, which is above the gel transition $\phi_c = 0.013$%w at 20°C and corresponds to a shear modulus $G = 1 - 260$Pa. The complex modulus $G = G' + iG''$ characterizes the rheology of agarose gels, which are known to have a loss modulus G'' that is many orders of magnitude smaller than the storage modulus G' over the range of frequencies used in the experiments [151, 104]. This implies that the gels behave as a linear elastic solid for the purposes of this study.

Surface waves were observed having a frequency f_o where $f_o = f_d/2$, as is expected for

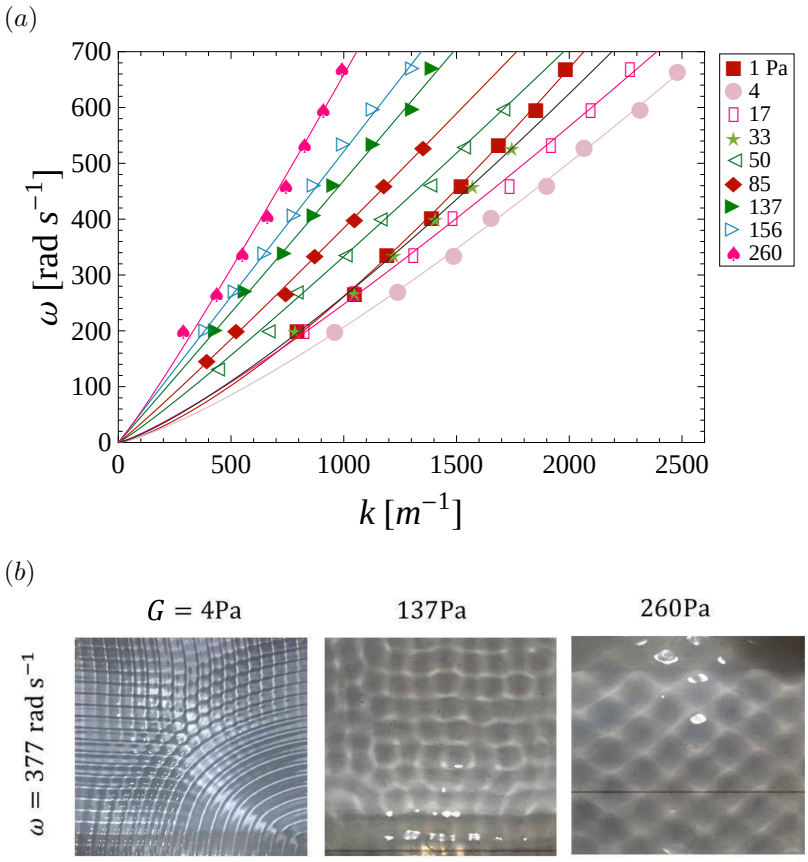

Figure 2.2: (a) Dispersion relationships plotting angular frequency ω against wavenumber k for a range of shear modulus G. Symbols are experimental data and lines are best fit power-laws. (b) Typical surface waves for $\omega = 377$rad s^{-1}, and $G = 4, 137$, and 260Pa.

Faraday waves[41, 12]. A strobe light is used to 'freeze' the wave surface, allowing us to obtain images at a fixed phase of the wave cycle, by setting the strobe frequency to f_o. Herein, I focus on the dispersion relationship and will refer to the wave frequency as $f \equiv f_o$. A fast Fourier Transform (FFT) technique was used to analyze the spatial structure of the wave pattern, from which an averaged wavelength λ was extracted. To eliminate edge wave effects, I crop the image to 0.8 times its original size.

2.3 Experimental results

The experimental protocol allows us to extract the dispersion relationship from the data (f, λ), as it depends upon the shear modulus G. Herein the results are presented in terms of

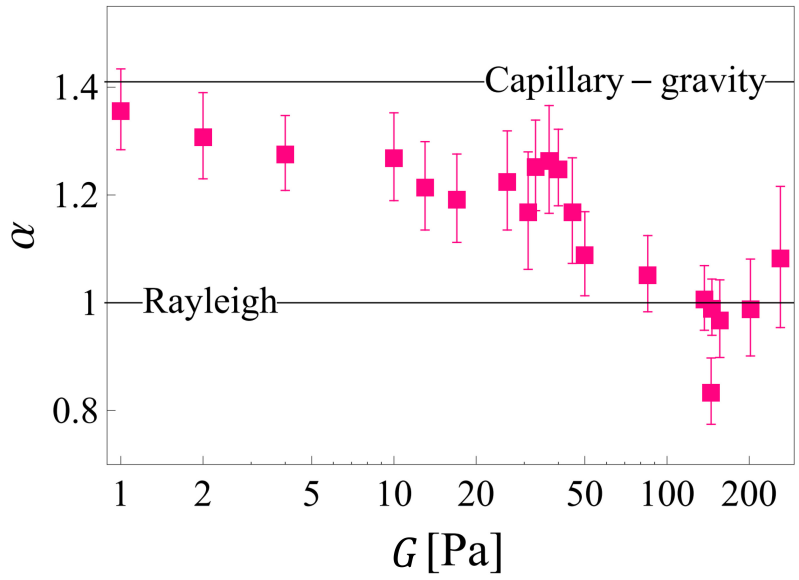

Figure 2.3: Power law exponent α fitted to experimental data against shear modulus G with limiting cases for Rayleigh $\alpha = 1$ and capillary-gravity $\alpha = 1.41$ waves annotated. Error bars represent 95% confidence intervals.

angular frequency $\omega \equiv 2\pi f$ and wavenumber $k \equiv 2\pi/\lambda$ to compare with the dispersion relationships for capillary-gravity (2.1) and Rayleigh (2.2) waves. For the ultra-soft agarose gels, I expect the dynamics to lie between these two extremes [104, 30]. The focus is on the role of the substrate elasticity G.

Figure 2.2(a) is a plot of the dispersion relationship, ω against k, for the range of shear moduli G explored here. Typical surface wave patterns are shown in Figure 2.2(b) for fixed frequency ω and three values of modulus G. The dispersion curves show the frequency ω is monotonic with wavenumber k, whereas the curves are non-monotonic with shear modulus G. This can be seen by ordering the curves by G as the graph is traversed from left to right; note especially that the experimental data for $G = 1$Pa lies to the left of the $G = 4$Pa curve. This observation highlights the interplay between elasticity and capillarity, as well as the prominent role of surface tension in gels with small G.

The raw experimental data is fitted to a power-law having the form $\omega = Ck^{\alpha}$, to gain insight into the transition from capillary-dominated to elasticity-dominated regimes. These curves are overlayed on the experimental data in Figure 2.2(a). Figure 2.3 is a plot of the power-law exponent α against shear modulus G with vertical bars equal to the 95% confidence interval for

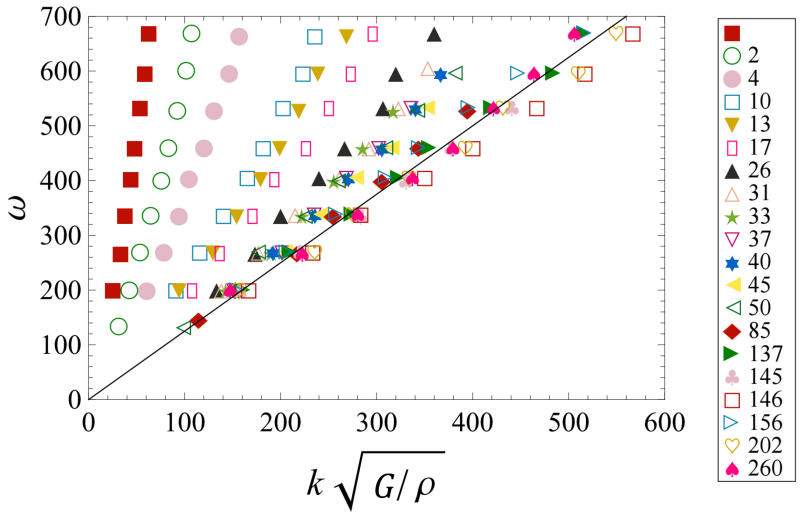

Figure 2.4: Rayleigh wave scaling (Eq. 2.2): angular frequency ω against $k\sqrt{G/\rho}$ shows a collapse of experimental data for shear modulus $G > 85$Pa. A best fit line for $G > 85$Pa is plotted to guide the eye.

each data point. For reference, capillary-gravity waves have a power-law exponent $\alpha = 1.41$ and Rayleigh waves $\alpha = 1$ over this range of frequencies. As seen in Figure 2.3, the majority of data lies within these bounding curves implying that both surface tension and elasticity are important to understand the dynamics. Note that gravity, which manifests itself through the self-weight of the gel, is an important factor in the dispersion relationship—pure capillary waves would have $\alpha = 1.5$. In the limit $G \to 0$ Pa, the waves behave as capillary-gravity waves, whereas for $G > 85$ Pa, the exponent $\alpha = 1$ within the 95% confidence interval (with the exception of one outlier) indicating Rayleigh wave behavior. In Figure 2.4, the experimental data is rescaled with respect to the form of the Rayleigh wave dispersion relationship (2.2) and show a collapse of the data for $G > 85$ Pa, implying that surface tension forces do not affect the dynamics in this "high" G regime.

So, while surface tension forces seem to become unimportant with sufficiently large G, the converse cannot be said for elasticity effects which are important even for small G. For example, as shown in Figure 2.3, it is not until $G = 1$Pa that α approaches 1.41.

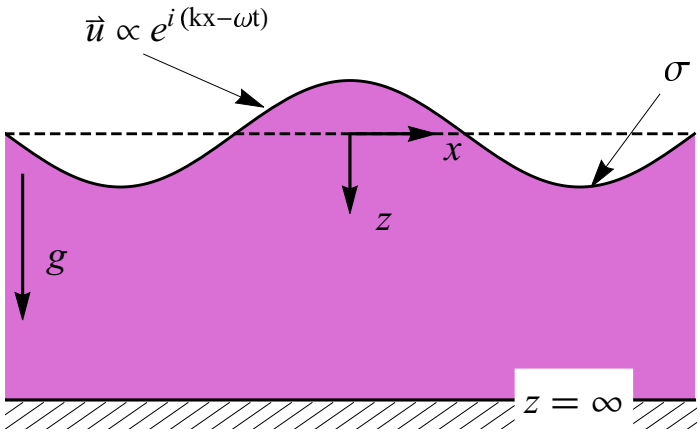

Figure 2.5: Definition sketch. A linear elastic solid occupies a semi-infinite half-space in the presence of a gravitational field g and has an interface $z = 0$ endowed with surface tension σ that is perturbed by a wave $\mathrm{e}^{i(kx-\omega t)}$.

2.4 Theoretical model

I am interested in developing a closed-form dispersion relationship to compare with the experiments, because existing theories of elastocapillary waves [52, 118] involve the solution of a complex nonlinear characteristic equation. I briefly sketch the details of this model, which builds upon the work of [118].

Consider a linear elastic solid that occupies a semi-infinite half-space and deforms due to its self-weight (gravitational constant g). The gel surface is endowed with surface tension σ and perturbed by a wave of the form $\mathrm{e}^{i(kx-\omega t)}$, as shown in Figure 2.5. The displacement field $\boldsymbol{u}(x, z, t) \equiv (u, w)$ obeys the elastodynamic Navier equations,

$$\rho \frac{\partial^2 \boldsymbol{u}}{\partial t^2} = (\lambda + G)\nabla(\nabla \cdot \boldsymbol{u}) + G\nabla^2 \boldsymbol{u} \tag{2.3}$$

where λ, G are the Lamé parameters. Continuity of stress τ is enforced at the free surface $z = 0$;

$$\tau_{xz} = 0,\ \tau_{zz} = -\sigma \frac{\partial^2 w}{\partial x^2} + \rho g w. \tag{2.4}$$

The first equation ensures the interface is free of shear stress, while the second is the Young-Laplace equation which relates the normal stress to the linearized mean curvature. The $\rho g w$ term is the disturbance to the pre-stress due to the gravitational body force or self-weight. Lastly, the solution

is required to be bounded $|\boldsymbol{u}| \to 0$ as $z \to \infty$.

To construct a solution to the field equations (2.3)–(2.4), the Helmholtz decomposition theorem is used to write the displacement field

$$\boldsymbol{u} = \nabla\phi + \nabla \times \boldsymbol{\psi} \tag{2.5}$$

in terms of the scalar potential ϕ and vector potential $\boldsymbol{\psi} = \psi\hat{j}$. Equivalently, $\boldsymbol{u} = (u, w) = (\phi_x - \psi_z, \phi_z + \psi_x)$ in component form. Sometimes ϕ and ψ are referred to as the compressional and shear wave potentials, respectively. Substituting (2.5) into (2.3) delivers a set of uncoupled equations,

$$\frac{\partial^2\phi}{\partial t^2} = \alpha^2\nabla^2\phi, \ \frac{\partial^2\psi}{\partial t^2} = \beta^2\nabla^2\psi, \tag{2.6}$$

where $\alpha \equiv \sqrt{(\lambda + 2G)/\rho}$ and $\beta \equiv \sqrt{G/\rho}$. Normal modes $\mathrm{e}^{i(kx-\omega t)}$ taking the form of steady waves propagating in the x-direction are assumed with k the wavenumber and ω the wave frequency. The solution of (2.6) is then given by

$$\phi = A\mathrm{e}^{-\gamma z}\mathrm{e}^{i(kx-\omega t)}, \ \psi = B\mathrm{e}^{-\delta z}\mathrm{e}^{i(kx-\omega t)}, \tag{2.7}$$

where $\gamma \equiv \sqrt{k^2 - \omega^2/\alpha^2}$ and $\delta \equiv \sqrt{k^2 - \omega^2/\beta^2}$ and (A, B) are unknown coefficients to be determined from the stress boundary conditions (2.4). Substituting (2.7) into the displacement form of the stress boundary conditions (2.4),

$$G\left(\frac{\partial u}{\partial z} + \frac{\partial w}{\partial x}\right) = 0, \ \lambda\frac{\partial u}{\partial x} + (\lambda + 2G)\frac{\partial w}{\partial z} = -\sigma\frac{\partial^2 w}{\partial z^2} + \rho g w, \tag{2.8}$$

gives a set of linear equation for the constants A, B,

$$\begin{bmatrix} i2k\gamma & 2k^2 - \frac{\omega^2}{\beta^2} \\ 2k^2 - \frac{\omega^2}{\beta^2} + \frac{\gamma}{\beta^2}\left(\frac{\sigma k^2}{\rho} + g\right) & -i2k\delta - i\frac{k}{\beta^2}\left(\frac{\sigma k^2}{\rho} + g\right) \end{bmatrix} \begin{bmatrix} A \\ B \end{bmatrix} = \begin{bmatrix} 0 \\ 0 \end{bmatrix}. \tag{2.9}$$

The resulting characteristic equation

$$4\sqrt{1-\frac{1-2\nu}{2(1+\nu)}c^2}\sqrt{1-c^2}-(2-c^2)^2 \\ +c^2\sqrt{1-\frac{1-2\nu}{2(1+\nu)}c^2}\left(L_e k+\frac{1}{L_g k}\right)=0. \tag{2.10}$$

is written with respect to the scaled Rayleigh wave speed $c \equiv \sqrt{\rho/G}(\omega/k)$, Poisson ratio ν, elastocapillary length $L_e = \sigma/G$ and elastogravity length $L_g = G/\rho g$.

The agarose gels used in the experiments can be considered incompressible $\nu = 1/2$ which allows the following simplification of the characteristic equation (2.10),

$$4\sqrt{1-c^2}-(2-c^2)^2+c^2\left(L_e k+\frac{1}{L_g k}\right)=0. \tag{2.11}$$

Note that (2.11) is a nonlinear equation for the wave speed c that depends upon the wavenumber k, elastocapillary length L_e and elastogravity length L_g. Assuming the agarose gels have solid surface tension close to that of water $\sigma = 72$mN/m, I estimate $L_e \sim 10^{-2} - 10^{-4}$m in the experiments. Similarly, $L_g \sim 10^{-2} - 10^{-4}$m but with the opposite trend of L_e implying there is range of shear moduli where $L_g \sim L_e$. Equating $L_g = L_e$ yields the critical shear modulus $G \approx 26$Pa, which is clearly in the transition zone between capillary-gravity and Rayleigh waves shown in Figure 2.3. A simple scale analysis between the surface wavelength $1/k$ and the elastocapillary length L_e gives capillarity-dominated $L_e \gg 1/k$ and elasticity-dominated $1/k \gg L_e$ regimes. In terms of the data set, the observed wavelengths for $G = 1$Pa are all an order of magnitude smaller than L_e and are capillary waves, whereas for $G > 85$Pa the observed wavelengths are an order of magnitude larger than L_e and are Rayleigh waves (cf. Figure 2.2). These scaling arguments are consistent with the transition zone $1 < G < 85$Pa shown in Figure 2.3. In the transition zone, both capillarity and elasticity affect the dynamics in a way that cannot be predicted a priori from scale analysis.

The disadvantage of (2.11) is that it is nonlinear and the dispersion relationship must be computed numerically. I seek to develop an approximate solution to more simply compare and analyze the experiments. I do this by series expanding Eq. (2.11) about $L_e k \ll 1$, keeping the lowest

order terms, and solving the resulting equation to deliver the dispersion relationship

$$\omega = \sqrt{\frac{2}{3}gk + \frac{2}{3}\frac{\sigma}{\rho}k^3 + \frac{4}{3}\frac{G}{\rho}k^2}, \tag{2.12}$$

It is noted that Figure 2.4 shows the experimental data collapses upon scaling with the Rayleigh wave dispersion, Eq. (2.2), for large $G > 85$Pa and the slope of that line is approximately 1.17, which is close to the predicted coefficient $\sqrt{4/3} \approx 1.15$, thus validating Eq. (2.12). For all the experimental data with the exception of $G = 1$Pa, $L_e k \leq O(1)$ and I expect Eq. (2.12) to be faithful. For $G = 1$Pa, however, $L_e k \approx 10$ and I might expect Eq. (2.12) to breakdown at this $L_e k \gg 1$ limit. This is confirmed by the fact that Eq. (2.12) does not recover the $G \to 0$ limit, Eq. (2.1). The advantage of Eq. (2.12) is a readily available closed-form solution for use in interpreting the experiments.

The experimental data is fitted to (2.12) treating surface tension σ as a parameter. Figure 2.6 is a plot of the resulting surface tension σ versus shear modulus G. The experimental data completely collapses in this case, as shown in Figure 2.7, which validates the use of the proposed dispersion relationship (2.12) in determining the surface tension of soft gels. The average value over the entire range of G produces $\sigma = 45.6$mN/m (cf. Figure 2.6). For reference, I show how the experimental data scales with the dispersion relationship (2.12) for this fixed surface tension value in the Appendix (Figure 2.8). Figure 2.6 shows the predicted σ values tend to become more scattered for $G > 137$Pa, which is firmly in the Rayleigh wave regime (cf. Figs 2.3,2.4) where the particular value of σ is largely irrelevant because of the dominant elastic forces. Other potential sources of scatter may include edge effects associated with large wavelength patterns in this regime and uncertainty in the shear modulus of the stiffest gel ($G = 260$Pa) which I have extrapolated from the data of [151]. Finally, It is noted the relatively large surface tension $\sigma = 83.2$mN/m predicted for the softest gel $G = 1$Pa, which I attribute to the range of validity of Eq. (2.12) mentioned above. It is concluded that (2.12) does a good job of predicting the experimental observations allowing us to extract the surface tension of soft gels, and may serve as a useful tool to other workers in this field.

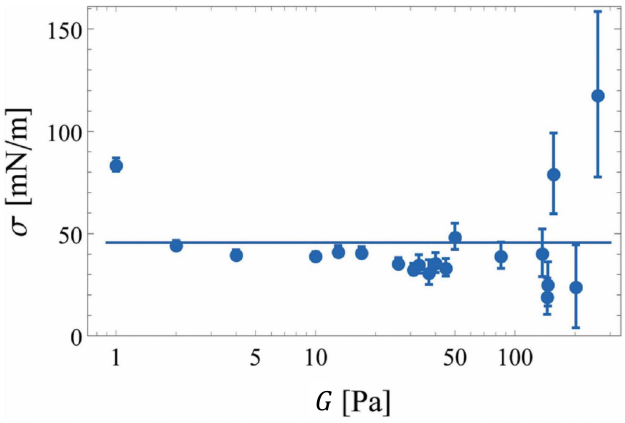

Figure 2.6: Predicted surface tension σ[mN/m] against shear modulus G[Pa] by fitting the dispersion relationship (2.12) to the experimental data. The average value over the entire range of G gives $\sigma = 45.6$mN/m. Error bars represent 95% confidence intervals.

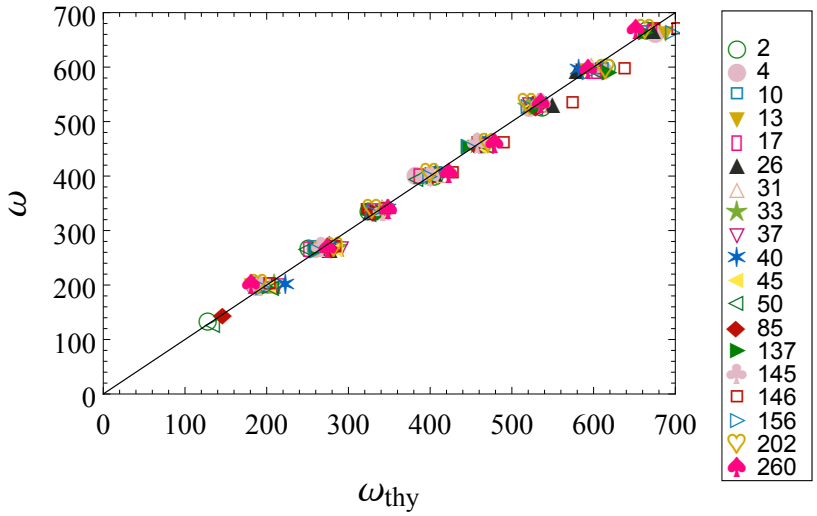

Figure 2.7: Elastocapillary wave scaling: angular frequency ω against proposed dispersion relationship ω_{thy}, Eq. 2.12, shows a collapse of experimental data for all shear modulus explored here.

2.5 Comparison to experimental data for average surface tension value

In Figure 2.7 I showed how the proposed dispersion relationship (2.12) collapsed the entire data set when treating the surface tension as an unknown parameter. The average value of surface tension over the entire data set was computed to be 45.6mN/m. Figure 2.8 plots the experimental data ω against the dispersion relationship ω_{thy} (2.12) using this value of surface tension, i.e. no fitting parameter. As shown, the comparison is worse than Figure 2.7, where I compute surface tension for each data set, but still does a reasonable job of reproducing the experimental results. The only significant exceptions are the limiting cases of $G = 1$Pa and 260Pa, where the predicted surface tension is furthest from that average value (cf. Figure 2.6).

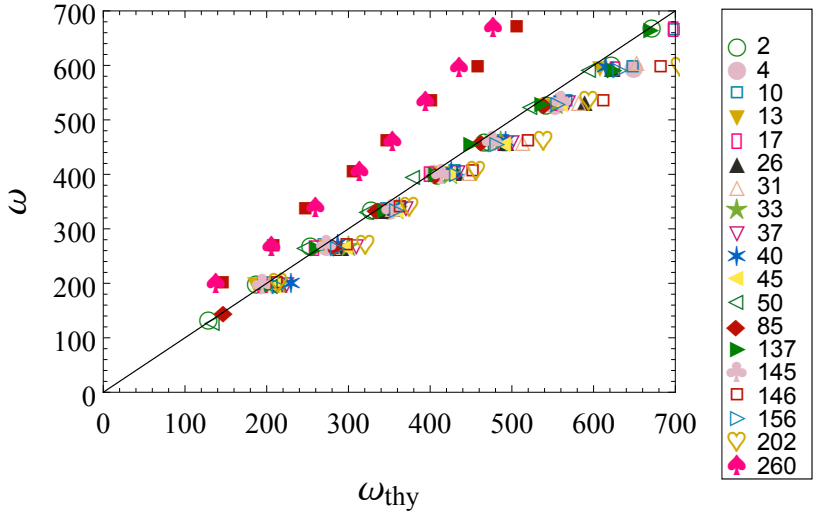

Figure 2.8: Angular frequency ω against proposed dispersion relationship ω_{thy}, Eq. 2.12, using the average surface tension value $\sigma = 45.6$mN/m for all G.

2.6 Discussion

Experiments of mechanically-excited surface waves on soft agarose gels are conducted and the dispersion relationship over a large range of shear moduli is characterized. Capillarity can dominate the dynamics for soft materials and the results capture the transition from capillary-gravity to Rayleigh waves as it depends upon the shear modulus. In addition, a new technique have

been developed to measure the surface tension of soft hydrogels by using a theoretical dispersion relationship for elastocapillary waves. It is expected that this new measurement technique, as well as the analysis of the dynamics of soft materials, to be highly relevant to a number of other technologies and to be useful to researchers working in the area of soft hydrogels.

Capillary instabilities in Newtonian fluids are widely used in industrial processes such as spray cooling, inkjet printing/rapid prototyping, turbulent mixing, and the float-zone method of crystal growth, all of which operate using the basic physical principles of the respective instabilities. For example, the formation of aerosols using vibrating transducers delivers drops with size related to the capillary frequency. Recent interest in technologies such as cell printing and tissue engineering use these basic principles but adapted to viscoelastic materials, such as bioinks [67, 145], which are typically hydrogels with complex rheologies (i.e. both liquid and solid properties) [35]. The agarose gels used in the experiments are also used in cell printing, making the results potentially applicable to the dynamics of pinch-off in single cell epitaxy [35].

Surface tension forces are important for gels with shear modulus $G < 137$Pa in the experiments, whereas elasticity affects the dispersion relationship for even the softest gels. In contrast, solid capillarity [3] can affect elastocapillary or soft wetting phenomena in much stiffer substrates; e.g. droplet spreading on silicone gel substrates with $G \sim 3$kPa can exhibit rich behaviors, such as stick-slip and stick-breaking motions, which are linked to the formation of a wetting ridge at the three-phase contact-line [122]. Viscoelastic effects can be expected to further complicate the dynamics of pattern formation in the experiments when the gel has a complex rheology. Future experiments could investigate the ability to control a dominant mode in viscoelastic gels for precise, robust and repeatable cell printing.

Chapter 3

Determining rheological properties of ultrasonically levitated gel drops

Reproduced from:

1. [Shao X, Fredericks SA, Saylor JR, Bostwick JB. Elastocapillary Transition in Gel Drop Oscillations. Physical review letters. 2019 Oct 31;123(18):188002] with the permission from American Physical Society;

2. [Shao X, Fredericks SA, Saylor JR, Bostwick JB. A method for determining surface tension, viscosity, and elasticity of gels via ultrasonic levitation of gel drops. The Journal of the Acoustical Society of America. 2020 Apr 22;147(4):2488-98] with the permission of AIP Publishing.

3.1 Introduction

The ultrasonic levitation of a drop has been used to obtain rheological properties of a substance for some time. Marston and Apfel[92] levitated a liquid drop in another immiscible liquid and excited the drop into quadrupole shape oscillations, showing how interfacial tension could be obtained from the resonance characteristics of these drops. This approach was later executed by Hsu and Apfel[60] who also developed an approach to account for finite viscosity effects and conducted preliminary measurements of changes in interfacial tension with increasing surfactant concentration on the drop surface. Further studies on surfactant measurements were conducted by

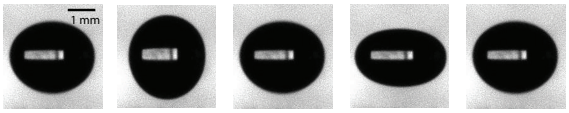

Figure 3.1: Typical drop oscillation over a cycle of period T. Note the static drop ($t = 0$) is slightly flattened (aspect ratio $W/H = 1.15$) due to the acoustic pressure required to levitate the drop.

Tian, Holt, and Apfel,[147, 148] who measured both the surface elasticity (not to be confused with the bulk elasticity examined herein) and surface dilational viscosity of surfactants on levitated drops. Trinh and Hsu[155] suggested the possibility of obtaining the surface tension σ of an ultrasonically levitated drop by measuring the outline of the equilibrium shape of the drop and extracting σ using the equation for the shape of a levitated drop due to the balance of the weight, acoustic radiation pressure, and surface tension. Trinh [156] showed that surface tension of an ultrasonically levitated liquid drop in air could be obtained by measuring the resonant frequency of the drop and extracting σ from Rayleigh's equation for the natural frequency of a spherical, inviscid liquid drop in air:

$$\omega_R = \sqrt{\frac{n(n+2)(n-1)\sigma}{\rho R^3}} \tag{3.1}$$

where n is the mode number, ρ is the density of the liquid, and R is the drop radius[79]. Of note is the fundamental $n = 2$ mode which has the lowest non-zero frequency and undergoes oblate-prolate oscillations, as shown in Figure 3.1.

Surface tension and viscosity can be obtained by ultrasonically levitating drops. This is typically done via one of two methods. The first, referred to as the finite decay approach, involves forcing prolate-oblate shape oscillations in the drop ($n = 2$ in Eq. (3.1), above) and then eliminating the excitation source and measuring the decay in drop oscillations. The frequency and damping constant of the decaying signal are then used to obtain surface tension and viscosity. This approach was reviewed and used in a recent publication by Kremer [74]. This approach was shown to be effective in measuring the difference in the blood viscosities of normal blood and the blood of individuals with sickle cell disease[57]. The second approach is termed the steady-state frequency response function where the modulation frequency is scanned through a range near the natural frequency of the drop and the response of the drop is observed. Both the surface tension and viscosity can be obtained by first obtaining the natural frequency and the damping coefficient from

the equation:

$$x = \frac{A}{\sqrt{\left(1 - \left(\frac{\omega}{\omega_n}\right)^2\right)^2 + \left(2\zeta\left(\frac{\omega}{\omega_n}\right)\right)^2}} \tag{3.2}$$

where A is the driving amplitude, ω and ω_n are the driving frequency and natural frequency, respectively, ζ is the damping coefficient, and x is the amplitude of drop oscillation. Obtaining ω_n and ζ from the experimentally obtained (x, A, ω) data, values for μ and σ can then be obtained from Lamb's equations for the $n = 2$ mode of spherical drop oscillation:

$${\omega_n}^2 = \frac{8\sigma}{\rho R^3} \tag{3.3}$$

and

$$\zeta = \frac{5\mu}{\rho R^2 \omega_n} \tag{3.4}$$

It is noted that Eqs. (3.3) and (3.1) are equivalent for $n = 2$. This approach has been used by Trinh and co-workers [152, 153], Hosseinzadeh and Holt[58], and others.

In the above investigations, liquid drops were studied which lack elasticity. Herein the rheological properties of a drop composed of a hydrogel which has significant surface tension, viscosity, and elastic modulus are studied. I am unaware of attempts to do this using ultrasonically levitated drops. It is noted that McDaniel and Holt[95] obtained the elasticity of aqueous foam drops via the acoustic levitation approach. Viscous dissipation and surface tension was not considered in that work.

The present work focuses on gels, specifically hydrogels. These materials, often referred to as soft solids, are unique in that both surface tension and elasticity can be roughly comparable in magnitude. Drops composed of a gel material, therefore, differ from the studies discussed above which concern liquids for which surface tension is essentially the only restoring force during drop oscillation since elasticity is negligible. Because gels are important materials in their own right, and also because they are often used as proxies for mammalian tissue, knowledge of the viscosity, surface tension, and elasticity of these materials is important. Herein the method of obtaining rheological properties of liquid drops and foams via ultrasonic levitation is extended to gel drops. While viscosity, elasticity, and surface tension are all important, only surface tension and viscosity are obtained by

the method presented herein, and elasticity is measured independently via a standard method. This is due to the moderate amount of noise in the system and the relatively small range in R in the drops studied; this precluded obtaining all three parameters although the theory developed herein enables this in principle. It is noted that surface tension, which is obtained by this method, is of especial importance, given that the standard Du Nüoy ring and Wilhelmy plate measurement methods[48, 1] are not possible for gels, since the measurement itself would break the gel.

3.2 Experimental section

3.2.1 Droplet levitation and modulating the acoustic force

The experimental setup used is illustrated in Fig. 3.2. As indicated, an ultrasonic transducer is used to levitate the gel drop. A camera and LED illumination source was used to image the gel drop and obtain its size, with the illumination source backlighting the drop. The transducer consists of a horn and reflector, following the general procedure of Trinh[154]. The horn and reflector are separated by an integer number of half wavelengths, with the drop levitated at one of the nodes. The pre-stressed PZT transducer used in the horn had a diameter of 3.5cm and was driven by an Agilent 33220A function generator, Kron-Hite amplifier (7500) combination. The function generator creates a sinusoidal carrier wave at the resonant frequency of the transducer, about 30.3 kHz, and this carrier wave was amplitude modulated at a range of frequencies near the resonant frequency of the drop, two orders of magnitude lower in frequency than the carrier wave. During an experiment, the AM frequency was swept from below to above the drop resonant frequency. A code written in LabView was used to control the drop levitation and AM frequency sweep. The AM frequency sweep typically took 3 minutes.

The transducer was initially tuned by adjusting the distance between the reflector and horn to most effectively levitate a drop. Then, the carrier wave frequency was adjusted to do the same. The process was iterated to achieve maximum levitation. From this point forward, resonance of the transducer could drift due to heating of the transducer and changes in temperature and humidity of the air. This drift would rarely exceed 10Hz, but was large enough to prevent effective levitation of drops. To address this, a software control in LabView was used to adjust the carrier wave frequency between AM frequency sweeps to maintain transducer resonance as shown in Fig. 3.3. The applied voltage and current to the transducer were measured with a Measurements Computing USB-2020

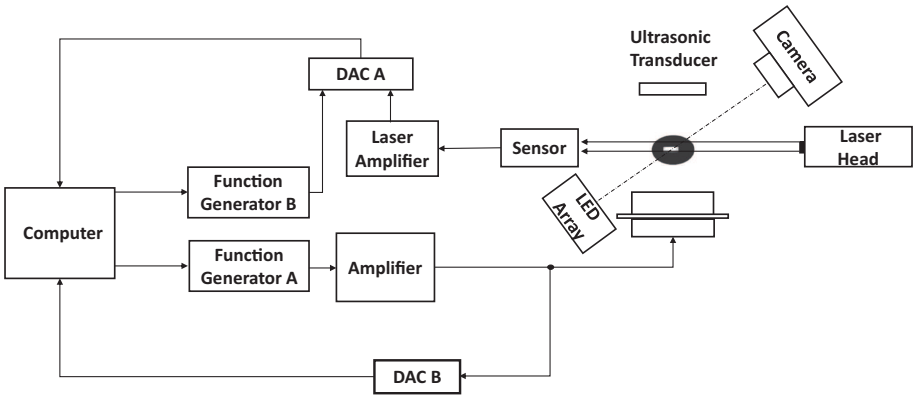

Figure 3.2: Schematic of the experimental apparatus

DAC at a sample rate of 10MHz. The phase shift α between these two signals was calculated, and the carrier wave frequency adjusted to keep α as close as possible to zero which maximizes the power applied to the ultrasonic levitation system. The carrier wave frequency was adjusted 3 times per second. The overall method for drop levitation is similar to that presented in Fredericks and Saylor[45].

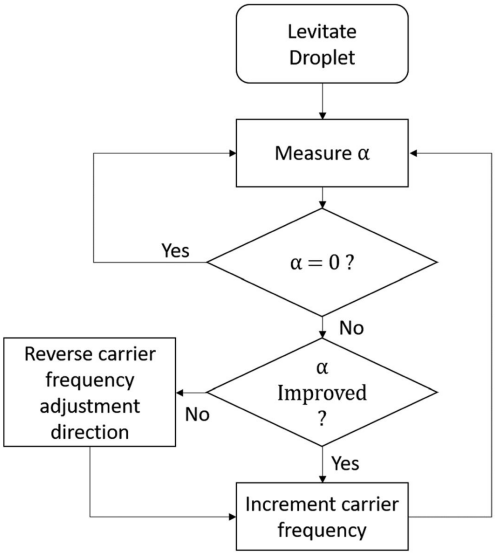

Figure 3.3: Flow chart illustrating method for adjusting the carrier wave frequency.

The amplitude of gel drop oscillation was measured using a laser light extinction approach similar to that of Marston[93], as shown in Fig. 3.2. A helium-neon laser beam (632.8nm wavelength) is expanded to ∼5 mm and directed at the levitated gel droplet. The resulting occluded beam strikes the detector of a laser sensor. This detector is actually a position sensitive detector with an x and a y output designed to report the centroid of the light striking the detector. However the unit also has a sum output that is proportional to the overall intensity of the light striking the detector, and this is the signal used herein. By placing a plate with a 3 mm diameter hole in front of the detector, this sum output is proportional to the fraction of the laser light that is occluded by the oscillating drop. The cross-sectional area of a levitated droplet should be proportional to its oscillation amplitude when oscillating in its quadrupole mode, and the frequency of the detector signal equal to the oscillation frequency of the levitated drop. For each frequency in the AM scan, 5 sec of data were acquired. Then the frequency was increased and another 5 sec of data were obtained. These frequencies were separated by 1 Hz, and during an experiment, a total of 30 frequencies were considered. The amplitude of the resulting drop oscillation at each excitation frequency was obtained by taking the FFT of the last 4 seconds of each 5 sec time trace. The first second of each trace was discarded to remove any influence of the previous AM frequency. The amplitude obtained from this FFT at the driving frequency is referred to as x and the amplitude of the driving frequency is referred to as A in Eq. (3.5) presented below. Each experiment resulted in a point in the plot of the amplitude of drop oscillation versus excitation frequency. The natural frequency was taken to be the frequency at which a maximum in drop oscillation was observed. This procedure was implemented in the Matlab programming environment.

3.2.2 Materials and methods

Following the approach of Tokita and Hikichi[151], hydrogels were prepared by dissolving agarose powder (Sigma Aldrich Type VI-A) in doubly distilled water[1] at 90°C for 1 hour at the desired concentration. The goal was to create gelled drops that were as close to spherical as possible. The drop is initially allowed to gel on a Teflon surface, and also experimented with letting the drop gel while ultrasonically levitated. However both of these approaches resulted in relatively oblate drop shapes along with significant changes in the drop size due to evaporation. Herein I followed the method of Aditi[25] and created a liquid mixture having a density gradient spanning the density

[1]Though Tokita and Hikichi used deionized water

of the gel. Specifically, I partially filled a beaker with silicone oil (PDM-7040, Gelest) having a density of $\rho = 1.07$ g/ml, and above this I poured n-octane (Acros Organics), having a density of $\rho = 0.7$ g/ml. Both silicone oil and n-octane are not miscible in agarose. The agarose solutions used had a nominal density of $\rho = 1.0$ g/ml and when placed in the beaker the agarose drops quickly migrated to the interface of the two liquids and exhibited a highly spherical shape. In addition to the resulting spherical shape, this approach also has the strength of allowing gelation without evaporation, ensuring that the agarose/water concentration did not change during gelation. After allowing these drops to gel at room temperature for at least 3 hours, a drop was removed from the silicone oil/octane beaker after which it was carefully washed in n-heptane (Fisher Chemicals) for 2 minutes to remove any excess silicone oil or octane. The drop was then washed once more with a fresh solution of n-heptane. After this, the drop was inserted into the levitation system and an experiment was initiated after allowing 15 seconds to pass so that any remaining heptane evaporated. Multiple drops were made from the same agarose solution ensuring that the concentration and hence the elasticity were the same when doing multiple runs. Drops made in this way were kept in the silicone oil/octane beaker until needed.

For each concentration of agarose gel used in these experiments, the complex modulus $G = G' + iG''$ for that gel was obtained using an Anton Paar rheometer (MCR 302). This method employs a small Petri dish in which the gel solution is placed and allowed to gel. The rheometer then contacts the surface of the gel with a disk. Dynamic oscillatory shear tests over a range of frequencies are then obtained. Prior to these measurements, a small amount of silicone oil was placed over the annular region between the disk and the edge of the Petri dish, preventing evaporation during the course of the measurement. For the gels used here, the loss modulus G'' is many orders of magnitude smaller than the storage modulus G'. Thus, the agarose hydrogels used in our experiments behave as linear elastic solids. For simplicity, the storage modulus G' is referred to as G hereinafter. For the gels investigated here, G ranged from 12.2 Pa to 200.3 Pa. The 95% confidence interval for measurement of G was 5.6 Pa which included the instrument uncertainty and experimental uncertainty obtained from measuring several samples of the same gel.

3.3 Theoretical model

Obtaining surface tension, elastic modulus, and viscosity, σ, G, and μ from the results presented above requires a model relating the driving frequency and drop oscillation amplitude, to the natural frequency and damping coefficient as was done for just σ and μ using Eqs. (3.2) - (3.4), in Section(3.1). This is done by developing an equation for the oscillations of a sphere having finite elasticity, viscosity, and surface tension.

The model follows that of Hosseinzadeh and Holt[58] by exploiting the similarity of the oscillating drop with the damped-driven oscillator

$$\ddot{x} + 2\zeta\omega_n\dot{x} + \omega_n^2 x = A\cos\omega t, \tag{3.5}$$

with ζ the damping ratio, ω_n the natural frequency and (A, ω) the driving amplitude and frequency, respectively. The harmonic oscillator structure of the field equations has been formally proven for liquid drops [16], rivulets [33, 18], and the more general capillary surface [17] using a boundary integral approach. Here the inertia acts as the 'mass', the resistive force of surface tension as the 'spring constant', and the combination of viscous and contact-line dissipation as the 'damping constant', all of which appear as operators that depend on the linearized surface deformation y. They become constants upon projection onto a particular interface shape. The drop oscillates in the fundamental mode $y(\theta, \varphi) = Y_2^0(\theta, \varphi) \equiv P_2(\theta)$, where Y_2^0 is the spherical harmonic of order $n = 2$ and index $l = 0$, and P_2 the Legendre polynomial [88], and I project onto this mode, which is axisymmetric and oscillates between an oblate and prolate shape.

Each component of the essential physics that enters into the model is schematically viewed as a spring or dashpot whose constant is normalized with respect to the drop mass. These relationships have been individually determined in the literature [129, 79, 39]. Damping is associated with viscous dissipation of a fluid which was computed by Lamb using the potential flow solution for the spherical drop [79]; this gives ζ in Eq. (3.4). Both surface tension and elasticity resist deformation like a spring and I idealize these two forces as springs in parallel so that I can superimpose their effects. The spring constant due to surface tension is given by Eq. (3.3) assuming an inviscid liquid drop [129]. The spring constant due to elasticity is computed from a nonlinear characteristic equation

$$\eta\left(\eta^2 - 10\right) j_2(\eta) - 2\left(\eta^2 - 16\right) j_3(\eta) = 0 \tag{3.6}$$

for the scaled elastic frequency

$$\eta = \omega R\sqrt{\rho/G} \tag{3.7}$$

with j_l the spherical Bessel function, assuming an incompressible spherical globe [39], which admits a numerical solution $\eta = 2.665$ that when rearranged gives the spring constant due to elasticity

$$\omega_n^2 = (2.665)^2 \frac{G}{\rho R^2}. \tag{3.8}$$

Note that there is no explicit coupling between surface tension and elasticity in the above development, and to our knowledge no such model exists for a spherical drop. Combining the spring constants due to surface tension and elasticity gives an effective spring constant

$${\omega_n}^2 = \frac{1}{\rho R^3}\Big[8\sigma + (2.665)^2 GR\Big], \tag{3.9}$$

which can be combined with the damping ratio ζ in Eq. (3.4) in the system response, Eq. (3.2). This enables a relationship between driving frequency and drop oscillation amplitude to (σ, ζ, G). Hence, by taking the driving amplitude, drop oscillation amplitude, and driving frequency data (A, x, ω) from any given gel drop levitation run and fitting it to Eq. (3.2) using ω_n and ζ as fitting parameters, the resulting (ω_n, ζ) can be obtained and used to get μ from Eq. (3.4), and G and σ from Eq. (3.9) by doing multiple runs with gel drops having different R.

3.4 Results

3.4.1 The elastocapillary transition in gel drop oscillations

Figure 3.4 plots the frequency response for a 1.54mm drop with shear modulus $G = 75$Pa. The curve shows a single peak at $f = 121.1$Hz which is the natural frequency for that particular drop. Note the peak exhibits a small bandwidth, indicative of weak viscous effects. The frequency response curves for the other gels similarly exhibit a single peak but at a different frequency. 66 experiments are performed to quantify the dependence of the natural frequency on G and R. The elastocapillary number $\Sigma \equiv \sigma/RG$ defines the relative importance of surface tension to elastic effects and its value ranges from $\Sigma = 0.22 - 21.07$ in the experiments.

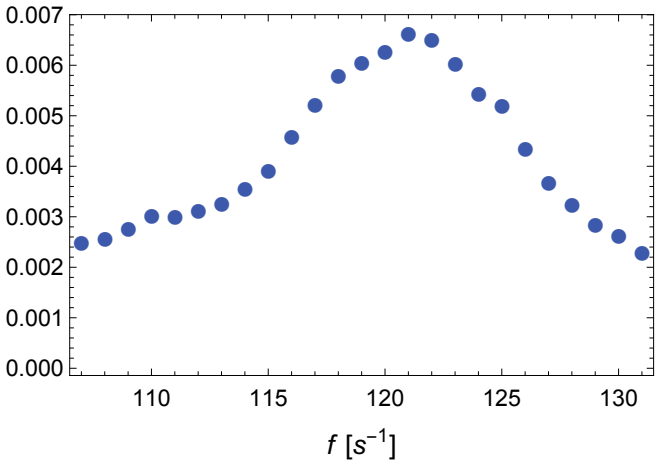

Figure 3.4: Frequency response plotting light intensity I against excitation frequency f for a $R = 1.54$mm drop with shear modulus $G = 75$Pa yields a resonance frequency of 121.1Hz.

Before analyzing the data further, it will be useful to discuss the physics of drop oscillations and the relevant scaling laws in the distinguished limits, elasticity $\Sigma \to 0$ and surface tension $\Sigma \to \infty$. This will be useful in interpreting the crossover between the two limits. The origin of any oscillation is the competition between inertia and a restorative force. For gel drops, both surface tension and elasticity resist deformation and it is natural to view these forces schematically as springs in a simple harmonic oscillator whose normalized spring constant k/m is simply the natural frequency squared $\omega_n^2 = k/m$ of the oscillator. Here the normalization is with respect to the inertia. I am interested in the $n = 2$ shape oscillations observed in the experiments. Unfortunately, no theoretical model of free drop oscillations exists in the literature which couples surface tension and elasticity, although [27] propose a model for sessile drops. There are uncoupled models for free drops that incorporate surface tension [129] and elasticity [39, 8] separately and I simply state those results. The natural frequency for an inviscid liquid drop held by surface tension is given by

$$\omega_\sigma^2 = \frac{8\sigma}{\rho R^3}, \tag{3.10}$$

whereas that of an incompressible elastic globe is

$$\omega_G^2 = C\frac{G}{\rho R^2}, \tag{3.11}$$

with different constants C reported in the literature. For example, a linear elasticity model for

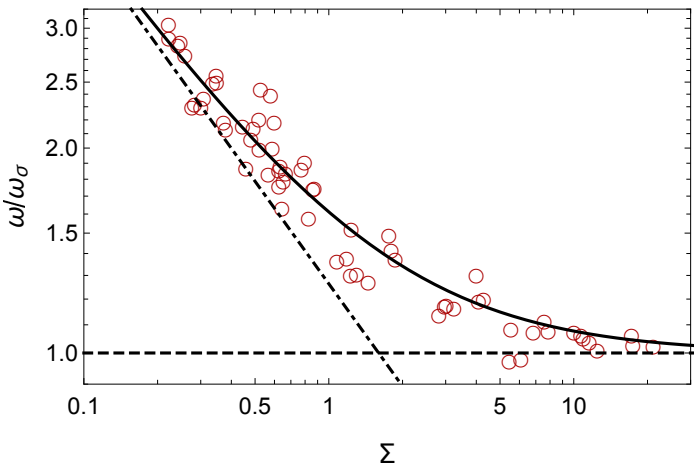

Figure 3.5: Scaled angular frequency ω/ω_σ against elastocapillary number Σ exhibits a transition between the capillary (dashed line) and elasticity (dot-dashed line) limits. The solid line is the best-fit composite expansion (3.12).

the spheroidal modes of oscillation predicts $C = 7.1$ [39], while a low-order approximate method of the continuum mechanics yields $C = 10$ in the low-frequency limit [8]. Prestress can also affect C. Henceforth, C is treated as a fit parameter noting that the scaling law remains unchanged. I expect to recover the appropriate scaling laws, (3.10) and (3.11), in the distinguished limits, $\Sigma \to \infty$ and $\Sigma \to 0$, respectively. The crossover between these two regimes is determined by setting $\omega_\sigma^2 = \omega_G^2$ which yields a critical elastocapillary number $\Sigma_c = C/8$ that separates capillary-dominated $\Sigma > \Sigma_c$ and elasticity-dominated $\Sigma < \Sigma_c$ motions. I am particularly interested in the crossover region where both surface tension and elasticity affect the oscillation dynamics. Using the oscillator perspective, surface tension and elasticity effects can be idealized as springs coupled in parallel and this coupling admits an effective natural frequency for the drop

$$\frac{\omega}{\omega_\sigma} = \sqrt{1 + \left(\frac{C}{8}\right)\frac{1}{\Sigma}}, \tag{3.12}$$

where I have scaled the frequency by the capillary frequency (3.10). This composite expansion yields an explicit dependence of the natural frequency on the elastocapillary number Σ. By construction, Eq. (3.12) recovers the limiting cases $\Sigma \to \infty$ (3.10) and $\Sigma \to 0$ (3.11).

I scale the experimentally-observed frequency by the capillary frequency (3.10), ω/ω_σ, and plot the entire data set against the elastocapillary number Σ in Figure 3.5. The results capture the transition between elasticity-dominated (dot-dashed line type) and capillary-dominated (dashed line

type) regimes and I recover the appropriate scaling laws in the respective limits. The data is fitted to the composite dispersion relationship (3.12) which yields a best-fit parameter value $C = 12.75$ which is slightly larger than that predicted by existing elastic theories $C = 7.1, C = 10$ [39, 8] but still reasonable. The order of magnitude agreement suggests the composite dispersion relationship (3.12) reproduces the essential physics and yields a critical elastocapillary number $\Sigma_c = 1.59$ using the data.

3.4.2 Extracting the rheological properties in gel drops

While experiments were indeed conducted at different R for gels of the same concentration, the range in R was small and increasing this range was challenging due to difficulties in forming small drops and in stably levitating large drops. This, combined with scatter in the data made difficult the extraction of (σ, ζ, G) from the experiments using the approach outlined above. Instead, G is measured as described in Section 3.2, and is used as an input while (σ, ζ) are extracted from the experimentally obtained (ω_n, ζ).

Figure 3.6 is a plot of drop oscillation amplitude versus driving frequency for a sample run where the elasticity of the gel was 32 Pa. The solid line in Figure 3.6 was obtained by fitting the data using Eq. (3.2). As noted in Section 3.2 the frequency at which the peak in this plot is observed is taken as the natural frequency. This peak was identified using the fit to the data as opposed to the data alone, since the fit incorporated information from multiple data points and was therefore less sensitive to a spurious measurement. In Fig. 3.6, the peak is located at a frequency of 99.32 Hz. It is also noted that while measurements were obtained at 30 excitation frequencies for each drop, only 21 were used (and presented in Fig. 3.6) because data points farther from the natural frequency tended to exhibit greater scatter. The y-axis in Fig. 3.6 is x/A where x and A are the same as presented in Eq. (3.5). As noted above, x is the magnitude of the peak in the FFT of the optical sensor data, and A the excitation amplitude.

The results of all the runs are presented in Figs. 3.7 and 3.8 showing how the natural frequency of the gel drop varies with G. In Fig. 3.7, the natural frequency is scaled to the capillary natural frequency given in Eq. (3.3), and is designated ω_σ in the figure. In Fig. 3.8 the natural frequency is scaled to the elastic frequency, Eq. (3.8), and is designated ω_G in the figure. The fact that neither Fig. 3.7 or Fig. 3.8 shows a plot where the scaled frequency is constant demonstrates that both surface tension and elasticity are playing a role in the gel drop dynamics, which is expected.

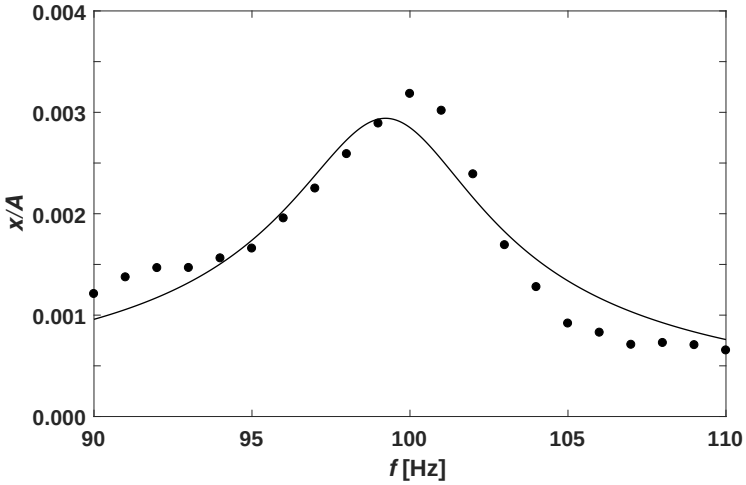

Figure 3.6: Plot of oscillation amplitude versus excitation frequency f for a sample run where the elasticity was $G = 32$ Pa.

It also shows that σ must be varying with the agarose concentration since a constant value for σ independent of that concentration (which would translate to a constant σ independent of G) should give a horizontal line in the plot of ω_n/ω_G in Fig. 3.8, which is not the case. As noted in Section 3.2, the 95% confidence interval for G was 5.6 Pa. Horizontal error bars are not included in Figs. 3.7 - 3.10 since this magnitude in uncertainty is so small, comparable to the width of the symbols in these figures.

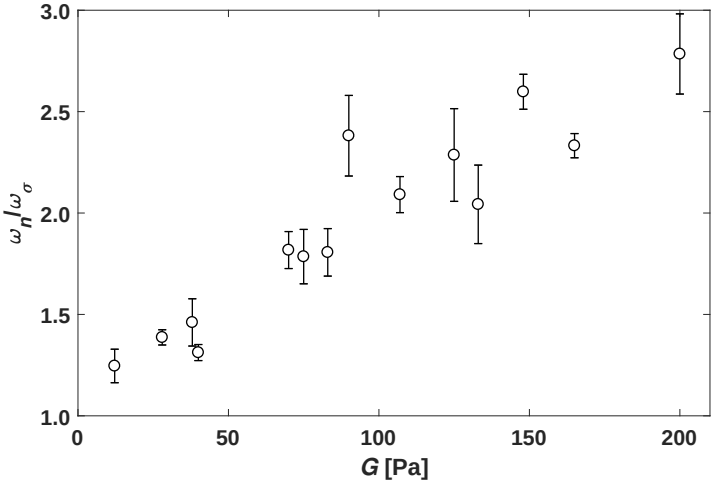

Figure 3.7: Plot of the gel drop natural frequency scaled to the capillary natural frequency versus elasticity G.

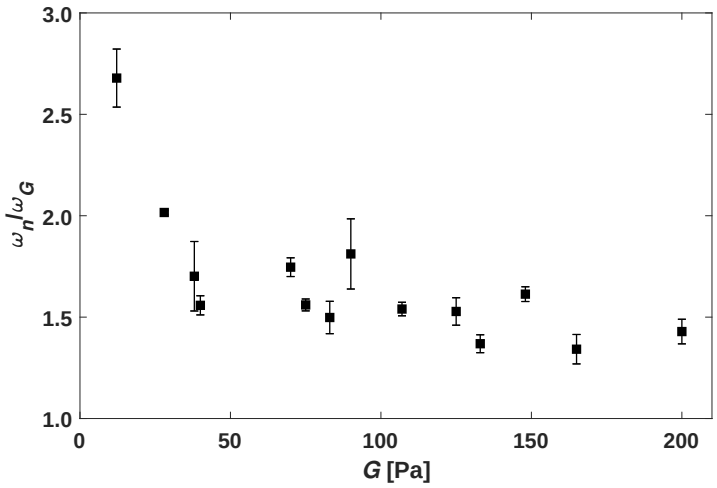

Figure 3.8: Plot of the gel drop natural frequency scaled to the natural frequency of a purely elastic drop versus elasticity G.

Applying the theory developed in the previous section, each data point presented in the above plots can be translated into a viscosity and surface tension, and these are presented in Figs. 3.9 and 3.10, respectively. The linear fits presented in Figs. 3.9 and 3.10, are:

$$\mu = 6.005 \times 10^{-5} G + 0.008384 \tag{3.13}$$

and

$$\sigma = 0.001022 G + 0.07229 \tag{3.14}$$

respectively.

It is noted that obtaining μ via the method described above is more sensitive to errors in data points that were far from the natural frequency. Hence, in obtaining μ, a total of 9 data points were used, the data point at the natural frequency and four above and below that frequency. This resulted in less scatter in the data than when using the entire data set since data farther from the resonance point was sometimes spurious in nature, occasionally exhibiting an amplitude higher than that at the natural frequency. This was not done when obtaining surface tension since, as shown in Eq. (3.9), σ depends on ω_n and not on ζ.

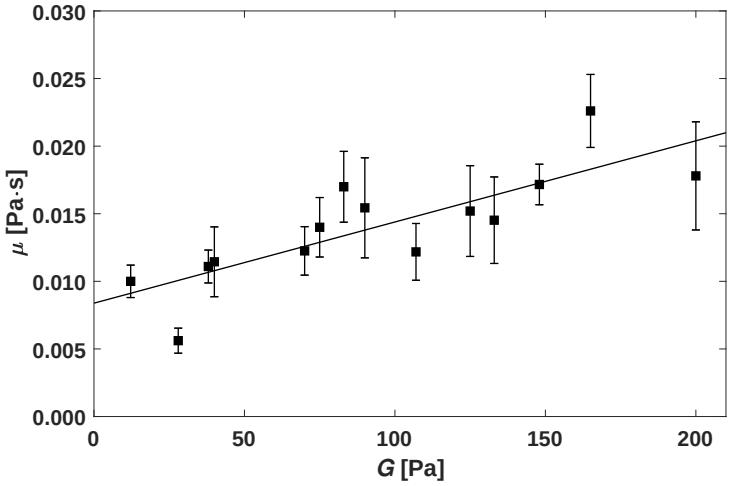

Figure 3.9: Plot of viscosity μ versus elastic modulus G with linear curve fit.

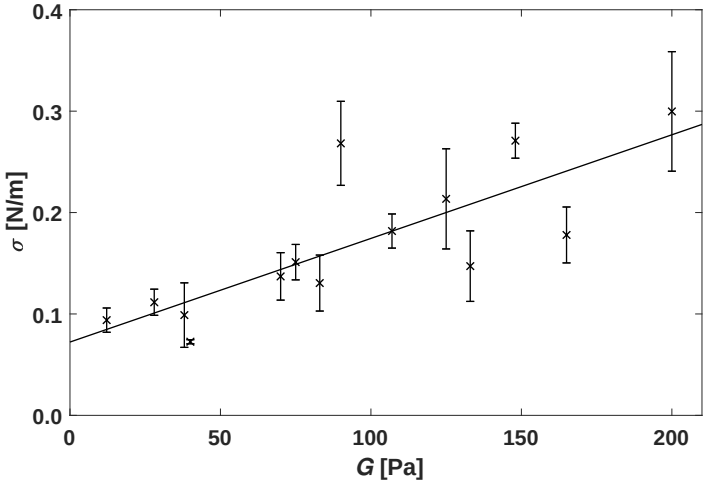

Figure 3.10: Plot of surface tension σ versus elastic modulus G with linear curve fit.

3.5 Discussion

The experimental observation of an oscillating gel drop over a range of experimental conditions where elastocapillary effects are important are reported. This is a canonical problem in elastocapillary dynamics and has the potential to impact this emerging field in the same manner in which the analysis of the Rayleigh drop has influenced the field of capillary dynamics, and associated applications, for more than a century. Scaling laws are recovered in the appropriate limits and a proposed relationship is shown for predicting the natural frequency of an elastocapillary drop,

that depends upon a nondimensional elastocapillary number, captures the essential physics in the crossover region. The experimental results yield a precise value of the elastocapillary number which delineates the elastic and capillary wave regimes. These results, as well as an interpretation of the physics, can help improve the aforementioned bioprinting and drop deposition technologies.

The experimental technique could also be used for material characterization of soft gels. Figures 3.9 and 3.10 demonstrate the ability of the described method to obtain (σ, ζ) for levitated gel drops. The ability to obtain σ is especially noteworthy since no other means have been reported for obtaining surface tension for a gel. Of course this also means that it is unable to compare the results to other data or methods. However, by setting $G = 0$ in Eq. (3.14), an extrapolated value of $\sigma = 0.0723$ N/m is obtained for the pure water case, which is essentially the exact value of σ for pure water at STP[162]. It is noted that the viscosity presented here is not the viscosity as it is typically understood, *viz.* the constant which relates the shear stress to the velocity gradient in a flowing liquid, since I am considering gels, which do not flow. Hence, μ is simply the quantity which accounts for energy dissipation in the deforming gel drop. Indeed, when $G = 0$ is set in Eq. (3.13), $\mu = 0.00838$ Pa·s is obtained which differs from the value of pure liquid water at STP by almost a factor of ten, a result which is likely due to the change in what μ in Eq. (3.4) represents when a liquid becomes a gel and ceases to admit flow, even at very small G. As noted in Section 3.3, only (σ, ζ) are obtained herein from the experimental data. It is possible to obtain (σ, ζ, G) from the data, taking advantage of small differences in R for the droplets used at each value of agarose concentration. However the range in R for these experiments was small, and the scatter in the data presented in Figs. 3.9 and 3.10 was not insignificant. A likely cause of the scatter is the low frequency oscillation (on the order of a few Hz) of the drop position within the ultrasonic standing wave field. Future work should focus on stabilizing the drop position, perhaps by including a shroud around the standing wave field and the development of a method for making gel drops capable of a large range in R. Success in these steps would enable obtaining measurements of (σ, ζ, G) via this method.

Lastly, it is noted that the dynamics of soft materials are naturally more complex than the statics due to the time scale associated with shape reconfiguration. The situation can become even more complicated for gels with a more complex rheology than the agarose gels used here due to the additional relaxation time scale, leading to interesting behaviors. This difference is readily seen in classical elastocapillary studies of static [66, 142, 15] and dynamic [69, 71, 122] wetting ridges with

the latter exhibiting complex stick-slip and stick-breaking behaviors. It is hopeful that this study inspires many follow on studies of dynamic elastocapillary phenomena to move this field forward.

Chapter 4

Edge waves on viscoelastic materials

4.1 Introduction

Mechanically-excited capillary-gravity waves can exhibit resonance when constrained in a finite tank, which is theoretically a boundary value problem with a series of eigenfrequencies[96, 23]. One method for forming these waves involves filling a tank and oscillating the tank in the vertical direction so that a pinned meniscus at the tank edge causes waves to propagate inward, in a direction normal to the tank edge. These waves have a frequency equal to that of the vertical tank oscillation, as long as the amplitude of vertial oscillation does not exceed the Faraday threshold, which is the case for the work presented herein. In a circular tank, the waves propagate inward, and reflect back out at the tank center. When the excitation frequency is tuned so that an integer number of wavenumbers exist in the tank, a standing wave will result and a fixed number of circular nodes form. As will be shown herein, this is a convenient method for experimentally determining the dispersion relationship for a material, since each observed mode represents a point in wavenumber-frequency space and can thereby be used to confirm such a dispersion relationship. This approach is somewhat similar to that of Saylor et al. (2000) wherein surfactant properties were obtained in a vertically vibrated cylindrical tank. In that work, wave slope was measured along a radial section of the wave field, and the wave slope along that line section was used to infer the surface tension of the interface.

Herein, full images of the circular wave surface were used, and the nodes identified and used to confirm the dispersion relationship and extract material properties; surfactants were not invetigated herein.

Both liquids and gels are investigated here. Due to the elasticity of gels, all other things being equal, the surface deformation of waves are smaller and the method developed herein is sensitive to very small deformations. Moreover, attempts to increase the deformation of gels could result in damage to those materials and hence these small amplitudes are in actuality desirable.

In this Chapter, the frequency responses of standing waves on water/glycerol mixtures and agarose gels are systematically studied in a circular tank and ascertain the effect of viscosity and elasticity on resonance. Agarose gel, a type of complex fluids characterized with a finite but relatively small elasticity, is the fundamental printing material for the emerging 3D bioprinting technology[114, 40]. Recent experiments report some capillary induced surface instabilities occurring on soft solids highlighting the elasticity effects in rearranging the threshold conditions, dispersion relationships and pattern formation behaviors of purely hydraulic instabilities [107, 105, 104]. These precursor experiments lead the subsequent interests in exploring the crossover between elasticity E and capillarity σ on soft solids defined as the elastocapillary length $L_e = \sigma/E$ entering the macroscopic region $L_e \sim 10^{-3}$m [26, 15, 136, 138]. These fundamental experimental shedding light to the unknown physics of the elastocapillarity on gels that is sometimes coupled with the hydraulic viscous effect, which is crucial to improve the precision and reliability of the current 3D bioprinting technology. The experimental protocol is outlined which characterize the resonance frequencies and corresponding amplitudes for the resonance modes on concentric meniscus waves on water/glycerol mixtures and soft agarose gels. A theoretical dispersion relationship is developed based on the governing equation of fluid mechanics with the appearance of surface tension incorporated as normal interface boundary, which can predict the resonance modes and amplitudes on viscoelastic materials by adding complex viscosity comprising viscosity part G'' and elasticity part G'. It is concluded that by highlighting the experiments and theory reveal the elasticity effect in changing the frequency response on capillary surface waves, which to our knowledge no previous literature has addressed.

It is noted that the general approach taken here where edge waves are used could also be extended into the use of Faraday waves which has been extensively studied[124, 12, 163, 42, 37, 31, 76]. However, the goal herein has been to determine if the dispersion relationship of a gel can be derived, confirmed experimentally, and then presented as a method for experimentally measuring

elasticity, surface tension, and viscosity. Due to the more complex dynamics inherent in Faraday waves, they were not pursued for this task. However, it is clear that a study of Faraday waves, including Faraday onset is an important future step since the richness of dynamics even for pure liquids is clear and hence the presence of elasticity in gels is likely to open more complex behavior.

4.2 Experimental procedure

Edge waves were investigated for glycerol/water mixtures and for agarose gels. The experimental setup used for this is presented in Fig. 4.1.

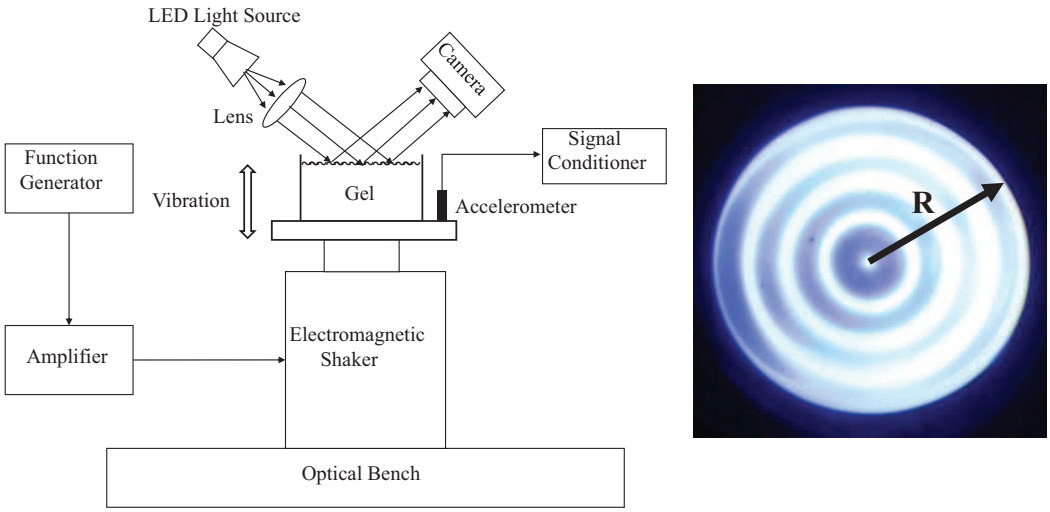

Figure 4.1: Schematic of the experimental apparatus used to obtain the frequency response of edge waves. An image of the typical wave pattern is presented in the inset.

The setup consists of a circular plexiglass tank of radius $R = 35$mm and depth $d = 22$mm mounted on a Labworks ET-139 electrodynamic shaker which provides vertical vibration of the tank, controllable in amplitude and frequency. Experiments were conducted for a range of driving frequency $f_d = 4.0 - 22.9$Hz. The shaker is driven by an Agilent 33220A function generator, Labworks PA-141 amplifier combination. The forcing amplitude of the shaker A was monitored using an PCB 352C33 accelerometer and a PCB 482C05 signal conditioner combination.

To characterize the wave pattern for a given liquid/gel and frequency, wave slope images

were obtained via the following procedure. A white light source was collimated by a lens located one focal length $f = 300$mm from the light source. To improve the degree of collimation, a plate with a 2 mm diameter hole was placed in front of the light source (a flashlight consisting of a white LED). This hole was located at the focal point of the lens providing a closer approximation to a point light source. The resulting collimated light beam was directed at the wave surface. The reflected light was captured by a digital camera (Canon EOS Rebel T3i, with a Canon EF-S 18-55 mm lens). The optical axis of the camera was oriented to coincide the reflection of the colllimated light beam from the flat fluid surface. In this way, when a wave field exists on the fluid surface, those locations where the slope is zero (peaks and troughs) exhibit a high intensity in the image whereas those regions where the wave slope is non-zero have a low image intensity. The more sloped the surface, the dimmer the image. Accordingly, the images presented herein are wave slope images where the intensity is inversely related to slope. This approach relies sensitively on the orientation of the camera optical axis with the spectral reflection of the collimated light from the flat surface. Similarly, it is dependent on the degree of collimation of the light source. To ensure that these conditions were met, images were periodically acquried of the flat, unexcited fluid surface, an example of which is presented in Fig. 4.2. This image, which is typical of these test images, has an average intensity $I = 250.5$ and an rms of ± 4.46, or $\pm 1.8\%$.

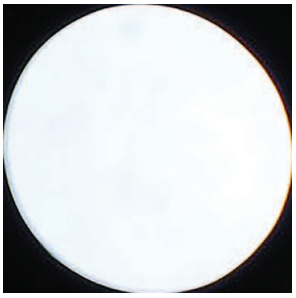

Figure 4.2: An example of reflection of the collimated light source as seen by the camera for a flat free surface.

To determine the locations in frequency space where resonant modes occur, frequency sweeps were performed for the liquids and gels investigated, vibrating the tank over a range of frequencies and obtaining a wave slope image at each frequency visited. To ensure that adequate resolution was obtaining in the region of resonance, a preliminary sweep was performed in each case, identifying the approximate location of the resonance frequencies. Then, the actual frequency sweep was conducted,

incrementing the frequency in 0.5Hz increments which shrink to 0.2Hz near the anticipated location of resonance. A wait time of 5 sec was imposed at each frequency before obtaining a wave slope image in order to ensure a fully developed wave pattern. A typical experiment took 30 minutes. The camera exposure was set to one second so that each image consisted of the integrated average of multiple wave periods. In this way, only standing wave modes resulted in a clear pattern and frequencies at which traveling waves exhisted were blurred over, revealing little structure to the image.

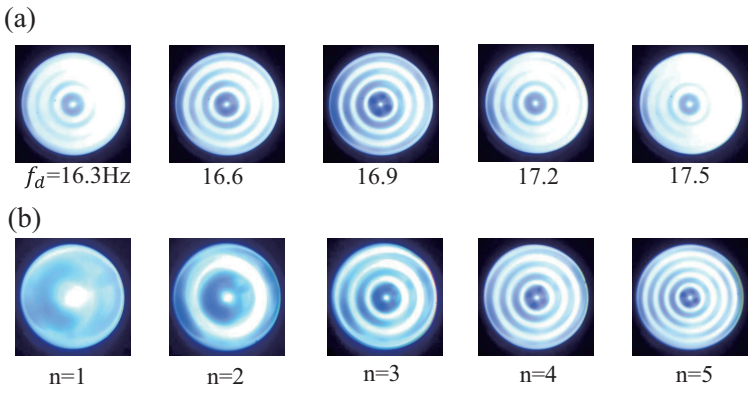

Figure 4.3: (a) Wave slope images for driving frequencies f_d =16.3Hz to 17.5Hz. Resonance is observed at $f_d = 16.9$Hz where a standing wave is attained for the $n = 4$ mode. Note that the image is progressively less clear as f_d deviates from 16.9Hz since the waves are not standing; (b) Wave slope images at the resonance frequencies corresponding to modes n=1, 2, 3, 4, 5. All images here are for water.

Figure 4.3(a) presents a sequence of wave slope images as the system approaches and departs resonance with f_d increasing from left to right. Here, resonance occurs at $f_d = 16.9$Hz which corresponds to the fourth resonance mode. The wave slope image for mode numbers n=1, 2, 3, 4, 5 are presented in Fig. 4.3(b). Note that the mode number n corresponds to the number of dark rings in the image. The bright regions are wear the standing wave alternates between being a peak and a trough, while the dark regions are the regions of maximum slope. The regions of maximum slope are the nodes, the locations where the surface elevation is unchanging.

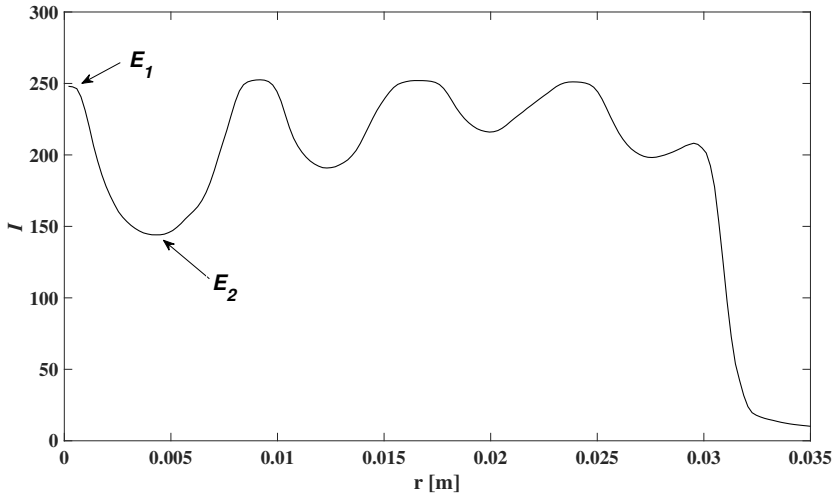

Figure 4.4: Plot of azimuthally-averaged light intensity I versus radius r. The maxima in the plot correspond to the flat locations on the wave pattern, i.e the locations where these standing waves oscillate between being a peak and trough during the course of a wave period. The minima in the plot are the nodes, locations where the wave slope oscillates between the largest positive and negative values. Arrows indicate E_1 and E_2, the intensities of the first two extrema in the I versus r plot, which are the intensities of the first flat region and the first node, respectively.

For each image of a resonant wave pattern, the light intensity I within the area of the circular tank in the image was azimuthally averaged to give an intensity I versus radius r plot, an example of which is presented in Fig. 4.4. The maxima on these plots correspond to locations in the wave field which oscillate between being peaks and troughs during the course of a wave period; locations in the actual wave pattern where the water surface is flat and most effectively reflects light to the camera. The minima on the I versus r plots correspond to the nodes of these standing wave fields, locations where the wave slope oscillates between a peak maximum slope and a peak negative slope. Stated another way, the minima in the I versus r plots are where the light reflected from the fluid surface has a direction that (referring to Fig. 4.1) oscillates from below the optical axis of the camera to above the optical axis of the camera and back again, during the course of a wave period.

It is desirable to quantify the overall amplitude of the wave field. Here I do this via the quantity $E_1 - E_2$, where E_1 and E_2 are intensities at the first and second extrema in the I versus r plot, as indicated in Fig. 4.4. The intensity E_1 is that of a flat surface and will attain a maximum

value, once resonance is attained. E_1 should approach the intensity of a flat, un-vibrated tank. And, at resonance, E_1 should differ little from the other peak intensities, since once the surface is flat, the intensity observed by the camera should be at its maximum. This is supported by Fig. 4.4 which shows that the peaks have more or less the same intensity of about 250. The intensity at the second extrema E_2 is that of the first node in the wave field and is the time integrated average of the intensity observed by the camera as the wave slope oscillates between a peak positive and peak negative value. The difference $E_1 - E_2$ is a good quantifier of the amplitude of the field because it should decrease away from resonance. Away from resonance, I have traveling wave patterns which average out over multiple wave periods to give an intensity field with lower peaks and higher toughs. On the other hand, as resonance approaches, the peaks attain their maximum flat surface value, while the troughs attain a minimum due to the fact that the sloped surface is directing light away from the camera's optical axis for most of the wave period. Of course $E_1 - E_2$ will also increase with the driving amplitude A, which is the max-min acceleration, measured in units of m/s^2. Since I wish to compare the intensity of the wave field at different frequencies without any sensitivity to the driving amplitude, the proximity of the wave field to resonance is characterized as X, where:

$$X = (E_1 - E_2)/A \tag{4.1}$$

Also, since there may be slight variations in the intensity of the light source and day-to-day deviations of the geometric setup of the camera and light source, E_1 and E_2 are both first scaled to the average intensity of the most recent flat image (e.g. Fig. 4.2) prior to insertion into Eq. (4.1). For each frequency sweep conducted, I identify the location of resonance frequencies as the locations of the peaks in plots of X versus f_d, an example of which is Fig. 4.6, presented in Section4.3.

Both liquids and gels were explored here. Specifically, glycerol/water mixtures having a range of volume ratios were explored, as well as agarose gels, linear elastic solids, over a range of agarose concentrations, giving a range of shear modulus. Doubly distilled water was used in preparation of both the glycerol/water mixtures and the agarose gels. The material properties of the five glycerol/water mixtures explored here are listed in Table 4.1. Agarose powder (Sigma Aldrich, Type VI-A) was used to prepare the hydrogels in the experiments. The powder was dissolved in doubly distilled water and kept at 90°C for an hour and then poured into the circular plexiglass tank. The concentration of the gel solutions ranged from $\phi = 0.06 - 0.13\%$w which corresponds to

Glycerol/water ratio	0:1	1:5	1:3	1:2	2:3	3:1
Surface tension (N/m)	0.0717	0.0702	0.0695	0.0687	0.0681	0.0658
Viscosity (mPa·s)	0.96	1.5	2.1	3.0	4.4	41.3
Density (kg/m^3)	1000	1045.4	1070	1093	1117.6	1202.4

Table 4.1: Material properties of the glycerol/water mixture ratios explored in this work.

a shear modulus $G = 2.6 - 13.2$Pa. The solution is allowed to gel at 25°C for 3 hours. The complex modulus of the agarose gels were measured using an rheometer (Anton Paar, MCR 302) which gave, for all gels in the experiment, a storage modulus G' many orders of magnitude larger than the loss modulus G'' implying that the gels in the experiments behave as linear elastic solids.

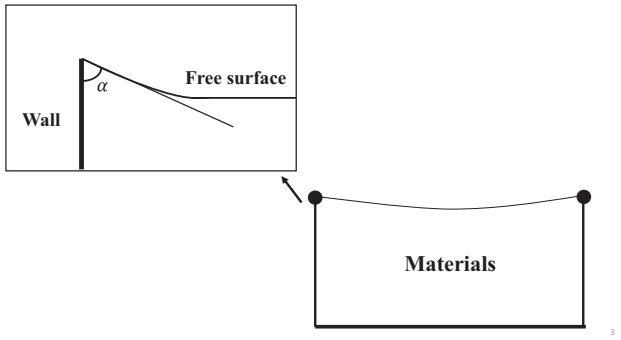

Figure 4.5: Illustration of the free surface showing the contact angle.

To ensure experimental repeatability, it is important to maintain the same contact angle α from run-to-run, where α is defined i Fig. 4.5. To ensure that this was the case, I first filled the tank with the glycerol/water mixture or gel solution so that the surface was pinned to the edge of the tank and was perfectly flat, giving a contact angle $\alpha = 90°$. This was checked by observing the image of surface giving a perfect uniform white field at the beginning of the experiment. A pipette was then used to carefully remove 2 ml of the fluid. This ensured the same contactt angle for each experiment.

4.3 Experimental results

The results from the glycerol/water mixture experiments are presented in Fig. 4.6 which is a plot of X versus f_d for the five different mixture ratios considered here, as presented in Table 4.1. Each of the frequency response curves presented in Fig. 4.6 exhibits several peaks each of which is located at the resonance frequency of one of the modes, with mode number increasing from $n = 1$ to $n = 6$ as f_d increases. Four general trends can be seen in Fig. 4.6.

1. For a given μ, as n increases the width of the peak increases.

2. For a given mode number n the peak shifts to the left with increasing μ.

3. As μ increases, the amplitude of each peak decreases.

4. As μ increases, the width of each peak increases.

The first observation shows that damping effects are positively correlated to the radial wave number. The second point, that for a given n, the location of the peak shifts to the left with μ proves this point again.

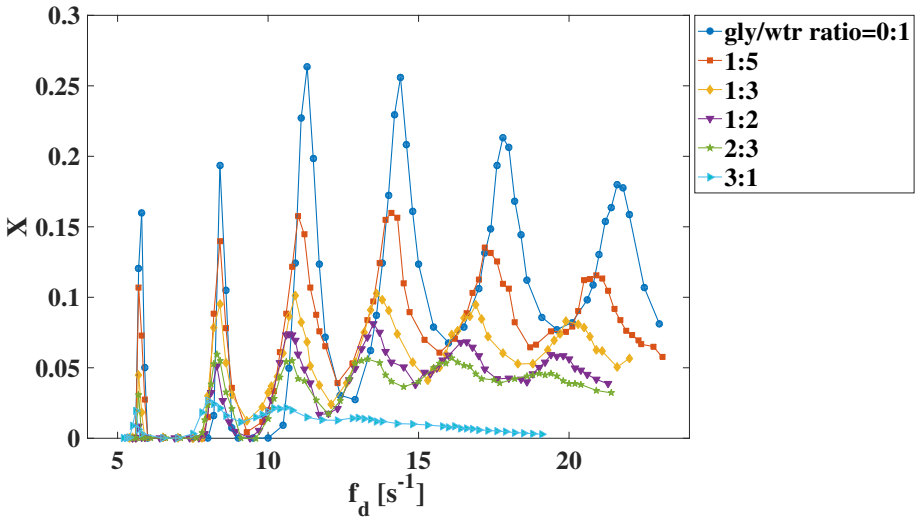

Figure 4.6: Frequency response plotting scaled wave amplitude against driving frequency f_d for concentric waves on the glycerol/water mixtures with glycerol/water volume ratio=$3:1, 2:3, 1:2, 1:3, 1:5, 0:1$.

To better explore the above observations, I plot in Fig. 4.7 X versus f_d for just the fourth mode. The decrease in amplitude, broadening, and leftward shift of these peaks with viscosity is characteristic of a driven damped harmonic oscillator. For concentric waves, surface tension and viscosity work as restorative force and damping respectively for the system. Comparing the curves for different μ, the resonant mode shift to lower frequencies with increasing viscosity and the magnitudes of wave amplitude X on each curve shows a monotonic decrease with μ. These observations highlight the damping effect of viscosity the dynamics.

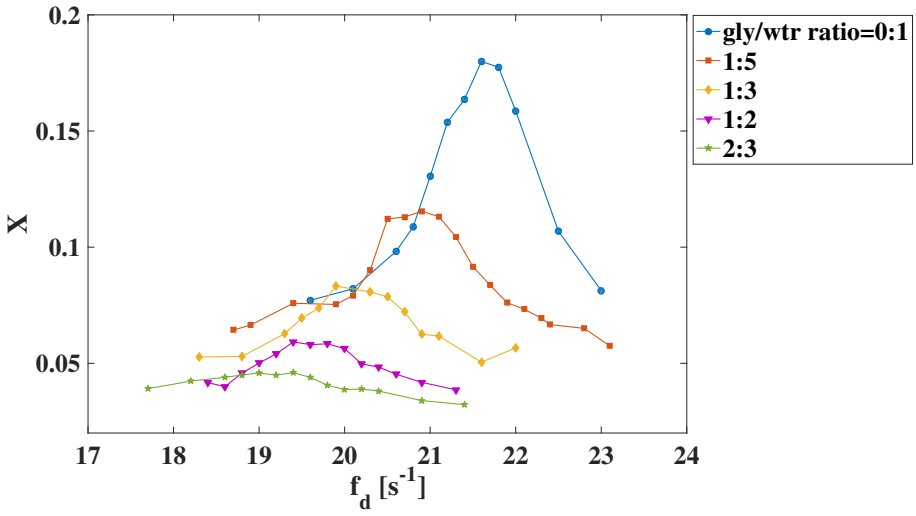

Figure 4.7: A plot of X versus driving frequency f_d for just the $n = 6$ mode of the data presented in Fig. 4.6.

By considering gels, materials with finite elasticity, a shift in natural frequency is expected to see due to a more robust restoring force existing in gels than the case for liquid where only surface tension serves in this capacity. Agarose gels behave as linear elastic solids, ideal for validating this hypothesis. Figure 4.8 exhibits the frequency response of edge waves on agarose gels with shear modulus G =1.2, 3.6, 8.4 Pa. Similarly to the liquids explored in Figs. 4.6 and 4.7, where the resonant mode frequencies shift to the higher locations with surface tension, here, the resonance frequencies shift to higher values as G increases. This can be attributed to the elasticity working as a restorative force and thereby shifting the resonance frequency of a dynamic system higher. Note the wave amplitude on the gels is much smaller than that of glycerol/water mixtures. Additionally, the wave amplitude decreases with n for gels, where it increased with n for most of the range of

n in the glycerol/water mixtures. These two observations imply a much stronger damping effect existing on gels which suggests a much higher viscosity for gels than for the glycerol/water mixtures. Note the frequencies for the first four resonance modes for G =1.2Pa are f_d =5.8, 8.5, 10.9, 13.0Hz which is fairly close to that of water f_d =5.7, 8.3, 11.0, 13.8Hz, but the wave amplitude X on water is about 10 times larger than the gel because of the larger viscosity. This interesting observation highlights the significance of elastic effects in the dynamics. So, I could say the elasticity effect which is important even for G as small as 1.2Pa which could still counterbalance a great viscous effect in shifting resonance frequencies.

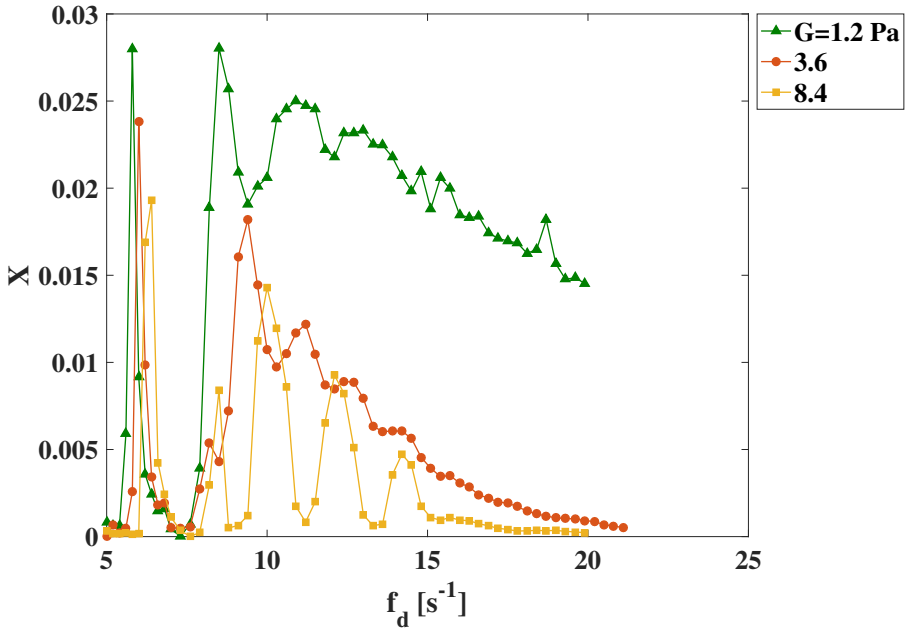

Figure 4.8: Frequency response plotting wave amplitude X against driving frequency f_d for concentric waves on agarose gels with shear modulus G =1.2, 3.6, 8.4 Pa.

Figure 4.9 is a plot of X versus f_d for $n = 2$ on agarose gels with shear modulus G =1.2, 3.6, 8.4, 15.3Pa respectively. The peak moves to higher frequency with increasing G. This follows the observation on Fig. 4.8. Whereas peaks in X vary non-monotonically with G, which indicates a positive correlation between viscosity and elasticity in agarose gels. A purely elastic response would have caused a monotonic increase in wave amplitude. This correlation between material properties can be proven by rheological measurements on agarose gels which shows the magnitude of storage

modulus G' which characterize the elasticity is always about 10 times than that of loss modulus G'' representing viscosity, regardless of the shear modulus.

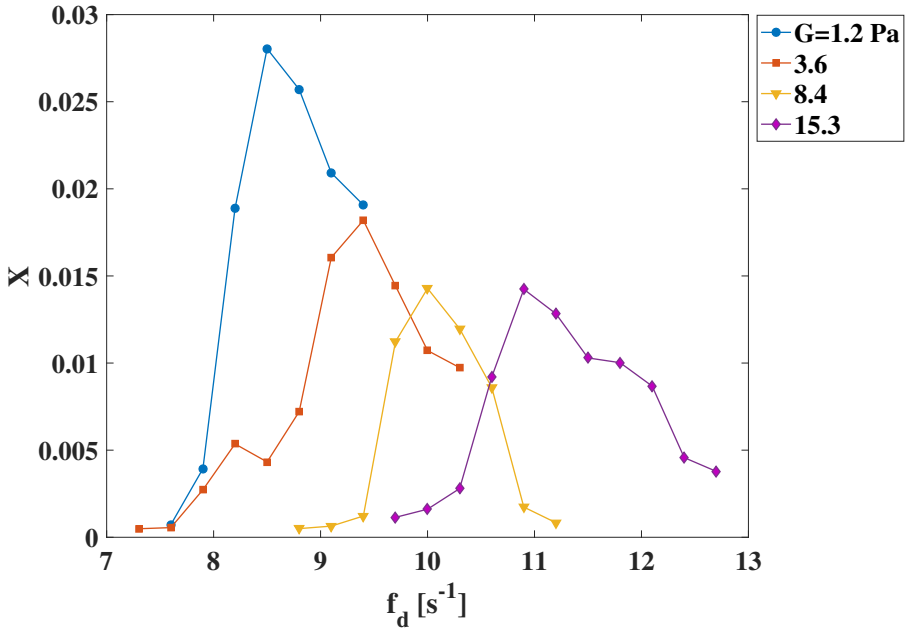

Figure 4.9: Plot of wave amplitude X against driving frequency f_d for the second resonance mode of concentric waves on agarose gels with shear modulus G =1.2, 3.6, 8.4, 15.3Pa.

4.4 Discussion

To better understand the relationship between mode frequency and viscosity, surface tension, and elasticity, a dispersion relationship is developed for surface waves on viscoelastic materials in Eq. (4.2). The following non-dimensional dispersion relationship, developed in the Appendix, is valid for both the viscous liquids and gels:

$$\lambda = i\mathbf{Oh}k^2 \pm \sqrt{\mathbf{Bo}k + k^3 + k^2\mathbf{Ec} - \mathbf{Oh}^2k^4} \tag{4.2}$$

1. $\lambda = \omega\sqrt{\rho R^3/\sigma}$, in which the wave frequency is scaled to the capillary time
2. Bond number $\mathbf{Bo} = \rho g R^2/\sigma$
3. Ohnesorge number $\mathbf{Oh} = \mu/\sqrt{\rho\sigma R}$

4. Elastocapllary number $\mathbf{Ec} = GR/\sigma$

The Ohnesorge number **Oh** in Eq. (4.2) defines the interplay between viscosity and surface tension effect in the dispersion relationship, the elastocapillary number **Ec** describes the elastocapillary effect, and the Bond number **Bo** representing the self-weight of the material which varies in a narrow range for the materials in the experiments. The wave number k is determined from the velocity condition at the side wall and is the root of the Bessel function J_1.

The resonance frequency f_d predicted by Eq. (4.2) for the first six modes on the six glycerol/water mixtures are compared with those obtained experimentally and listed in Table 4.2. **Oh** ranges from 0.00064 to 0.0145, $\mathbf{Ec} = 0$, and **Bo** has a relatively narrow range from 170.8 to 223.7. The shift of resonance frequency for different glycerol/water mixtures illustrated in Fig.4.6 is mainly a consequence of **Oh**. The differences between the experiments and theory are within 10% in Table 4.2, which suggests Eq. (4.2) can predict the surface waves dispersion relationship on a wide range of viscous liquids reasonably well.

The resonance frequencies f_d for the first four modes on gels from Eq. (4.2) are compared with experiments on the 4 gels whose properties are listed in Table 4.3. The gels in the experiments are treated as inviscid solid thus giving **Oh**=0 and assume surface tension on gels σ=0.072N/m. **Ec** ranges from 0.585 to 7.469 for the four gels. The wide range of **Ec** enables us to explore the elastocapillary effect in the dispersion relationship. **Bo** is equal to 170.8 for all the gels. In Table 4.3, the theory predicts the first three resonance frequencies pretty well and the differences are within 10%. However, the differences are relatively high for the $n = 4$ mode. It is assumed that the difference comes from the inviscid hypothesis in our model, which gives more discrepancy on higher resonance mode where the viscous effect can be more important. In addition, nonlinear effect is observed in the dispersion relationship on gels. Two $n = 2$ modes are observed on G=8.4 Pa and this multiple appearance of $n = 2$ mode has been observed consistently for gels with $G \geq 3.6$ Pa. The existence of nonlinear effect can add more complexity in defining the mode number, which can definitely give rise to the error to the comparison.

4.5 Conclusion

The frequency responses for edge waves in glycerol/water mixtures and gels are experimentally studied, in which the surface tension, viscosity, and elasticity effects are characterized in shifting

Glycerol/water ratio	Oh	Ec	Bo	n=1	n=2	n=3	n=4	n=5	n=6
0:1	0.00064	0	170.8	3%	4%	1%	3%	3%	4%
1:5	0.00093	0	182.4	2%	0%	3%	3%	6%	6%
1:3	0.00129	0	188.6	2%	0%	3%	6%	6%	9%
1:2	0.00184	0	194.9	2%	0%	4%	6%	7%	9%
2:3	0.00267	0	200.9	2%	0%	4%	6%	7%	10%
3:1	0.0145	0	223.7	1%	2%	4%	6%	OD	OD

Table 4.2: Comparison of resonance frequencies of edge waves from Eq. (4.2) and experiments on glycerol/water mixtures.

G (Pa)	Oh	Ec	Bo	n=1	n=2	n=3	n=4
1.2	0	0.585	170.8	2%	2%	7%	15%
3.6	0	1.757	170.8	3%	5%	6%	21%
8.4	0	4.100	170.8	5%	5%	3%	17%
15.3	0	7.469	170.8	7%	9%	4%	12%

Table 4.3: Comparison of resonance frequencies of edge waves on gels from Eq. (4.2) and experiments

the resonance amplitude and resonance frequency. A non-dimensional equation is also proposed for predicting surface wave dispersion relationships on viscoelastic materials, which relates surface tension, viscosity, and elasticity to the two non-dimensional number **Oh** and **Ec**. The comparisons of the resonance frequencies obtained from experiments and theory indicate the theory can predict the dispersion relationships very well for most of the materials. The relatively large discrepancy on $n = 4$ mode on gels are resulted from the inviscid hypothesis on gels is not able to predict the relatively larger dissipation in higher modes and the nonlinear effect makes the mode number definition difficult.

It is noted the role of **Ec** in shifting the resonance modes for edge waves on gels is similar to that on gel droplets in Chapter 3. Both of the resonances for a gel droplet and the gel edge waves are shifted to higher frequency with increasing **Ec**. This suggests that the surface tension and elasticity should also work as the restorative force in the edge waves system. In Chapter 3, a higher viscosity is extracted from the frequency response curve of a gel drop with wider bandwidth. This observation also follow the edge waves results in Fig.4.6 where wider bandwidths of the frequency response curves are obtained on higher viscosity mixtures. For edge waves, the viscosity effect is studied in shifting the resonance modes as the dissipation of the system. These results are considered as the complementary study to Chapter 3 and further interpret the interplay of surface tension, elasticity,

and viscosity in the dynamics on gels.

Lastly, in Fig.4.8 two $n = 2$ modes are observed on G=8.4 Pa; The first $n = 2$ mode at f_d=8.5 Hz and the second $n = 2$ at f_d=10 Hz. This indicates possible nonlinear effects in gels. It is noted that the first $n = 2$ mode frequency is very close to that of water $f_d = 8.4$Hz and the second $n = 2$ mode is close to the prediction from Eq. (4.2). This could indicate purely surface tension induced resonance mode is obtained in the first $n = 2$ mode and the emergence of the second $n = 2$ mode is determined by the coupling of elasticity and surface tension. The result highlights the complex interplay of surface tension and elasticity in gels and bears further investigation. This observation is generally true for gels with $G \geq 3.6$ Pa.

Chapter 5

Faraday waves on viscoelastic materials

5.1 Introduction

Pattern formation phenomena are ubiquitious in numerous fields including physics [49], biology [97, 63], and geology [73, 5]. For example, patterns of pathogen adhesion to host cells suggest the mechanism of onset of infection [83] and the revelation of striped pigmentation patterns on zebrafish skin shed light in the study of genetics [89]. Recently, innovative work in regenerative medicine has employed biocompatible polymers to print tissue scaffolds, which are typically hydrogels, e.g., agarose and alginate, and used to support cell growth in damaged organs [167]. Faraday waves are a canonical example of pattern formation on liquid surfaces [14, 123, 124]. In this chapter, mechanical-excited surface waves are used to study the pattern formation on ultra-soft agarose gels with a shear modulus range $G = 0.4 - 12.2$Pa. The onset of Faraday waves and the corresponding wave pattern are characterized and the effect of elasticity in shifting the Faraday waves tongues is revealed by comparison with pure liquids. A table of mode shapes is constructed from the experimental observation of the first 50 resonant modes. The observation of Faraday waves in soft gels has not been previously observed, to our knowledge.

Faraday waves are parametrically excited surface waves that are generated by vertical oscillation of a fluid-filled vessel[42]. In most Newtonian fluids, these are subharmonic waves that oscillate

at half the external driving frequency [150, 111]. However, if the layer is sufficiently thin and the driving frequency is low, a harmonic response has been reported [112]. Various wave patterns, such as stripes, squares, and hexagons have also been observed for different fluids and driving frequencies [75]. For some special cases, rotating spiral wave patterns have been observed on a circular container when the near wall shear stress disturbs the bulk flow [72], and a quasi-harmonic pattern can be excited with two frequency forcing introduced simultaneously [38].

A threshold in forcing amplitude accompanies the emergence of a Faraday wave pattern, and a fixed wave pattern is observed for each mode. The early experiments of Benjamin and Ursell showed an "instability tongue" in the driving amplitude-frequency space, the shape of which is determined by the Mathieu equation[12]. The minimum amplitude of the tongue occurs at the natural frequency of that wave mode. Bechhoefer [10] and Douady [36] observed multiple instability tongues which highlight the importance of the mode discretization on Faraday waves in containers. Due to viscous damping, the threshold tongues can be shifted to higher amplitude and lower frequency[12, 53]. The source of damping includes viscous dissipation at the surface, boundary layers at the bottom and the sidewall, and the moving contact line on the sidewall [157, 102], the combination of these different phenomena makes the modeling extremely challenging. Sorokin added linear viscous damping into the Mathieu equation, which turned out to be much smaller than the experimentally measured threshold values by Brand and Nyborg [157, 38]. To address the discrepancies attributed to damping effects in the system, efforts have been made to design idealized experiments which could create free slip sidewall conditions. Bechhoefer [10] developed a Faraday waves setup by using a highly viscous fluid to eliminate the effects of sidewalls, which agreed fairly well with sidewall stress-free viscous linear theory from Kurmar and Tuckerman [77]. Baston [9] produced an experiment which suppressed the sidewall stress and enabled them to appropriately compare the measured threshold with the theory of Kumar and Tuckerman.

There is comparatively very little literature on Faraday waves on viscoelastic materials where elastic effects are significant. Wagner observed a variety of novel coexisting wave pattern on polyacrylamide-co-acrylic acid [159]. Kumar theroetically analyzed the critical amplitude for Faraday waves on viscoelastic fluids and suggested a harmonic response could be observed when the elastic force is relatively strong when compared to surface tension and the driving frequency is close to the liquid relaxation time [78]. More recent work has used planar Faraday waves to study the elasto-capillary dispersion on soft solids [138]. Despite these preliminary studies, the role of elasticity

in pattern formation on Faraday waves is still not clear. As stated earlier, successful prediction of the onset of surface instability on gels is crucial to improve the 3D bioprinting resolution [40]. The goal of this chapter is to experimentally characterize the effect of elasticity on the shape of Faraday instability tongues for gels with shear modulus $G = 0.4 - 12.2$ Pa. In comparison, the Faraday instability tongues are also studied on water and glycerol/water mixtures in the same experimental setup to determine the viscosity and surface tension effect in the system. These complementary experiments demonstrate how viscosity, elasticity and surface tension affect Faraday wave pattern formation phenomena.

5.2 Experimental Procedures

Faraday waves are excited on soft agarose gels in a circular container with radius $r = 35$mm and height $H = 22$mm, as shown in the vibration system in Fig. 5.1. The container is filled to the edge to ensure a 90° contact angle between the surface and sidewall. A function generator and amplifier combination is used to generate the vibration on an electromagnetic shaker for a range of forcing frequencies and amplitudes. An accelerometer is installed perpendicular to the container to measure the vertical acceleration of the shaker. For a given Faraday wave mode, a frequency sweep is performed with driving frequency interval $I = 0.2$Hz. The threshold amplitude for a given frequency is measured using a laser light system for the surface wave response. A helium-neon laser beam (632.8nm wavelength) is directed to the free surface and reflected to the detector of a laser sensor, which gives analog voltage output proportional to the position of the centroid of the light striking the sensor in Y-direction. The time traced output signal is transmitted to an oscilloscope and processed immediately through a FFT operation. The main frequency of the time traced signal is obtained which corresponds to the dominated surface frequency. In the experiment, the wave frequency measured is always identical to the driving frequency $f_o = f_d$ in the beginning of each experiment, which indicates meniscus waves are excited from the sidewall of the container. The Faraday wave threshold is approached by increasing the output amplitude from the amplifier until the rapid growth of frequency peak at $f_o = 0.5 f_d$ is observed, which is a signature of Faraday waves. The corresponding output amplitude A_u is the upper limit of the threshold amplitude in that driving frequency. I then decrease the amplitude until the moment that the frequency peak on FFT disappear and note this the lower limit of the threshold amplitude A_l. The threshold amplitude lies

between A_u and A_l . The amplitude sweep operations are iterated several times until the difference between A_u and A_l is smaller than 0.2m/s^2. The experimental obtained threshold amplitude is computed as the average value $A = (A_u + A_l)/2$.

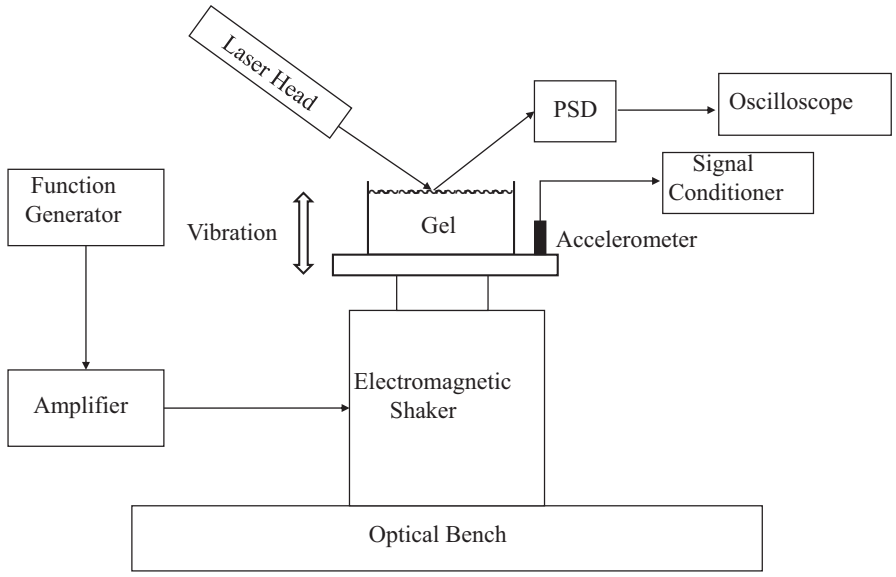

Figure 5.1: Experimental setup

An optical system consists of a white flash light, a convex lens and a camera (Canon EOS Rebel T3i) is developed to capture the slope of the Faraday waves pattern which is used to characterize the spatial structure, as illustrated in Fig. 5.2. A white flash light is placed at the focal point of a convex lens ($f = 300\text{mm}$) to produce collimated light and the beam is wide enough to illuminate the entire free surface. The images are obtained by setting the camera to be oriented normal to the reflected light. A long exposure time $t = 0.6\text{s}$ is used to distinguish the Faraday wave pattern from those traveling parts originated from the sidewall.

A typical image of Faraday waves pattern observed in a circular container is shown in Fig. 5.3 and exhibits a spatial structure defined by a radial mode number n and polar mode number l. The 2-D cross correlations are computed between the wave pattern image and a table of Bessel functions

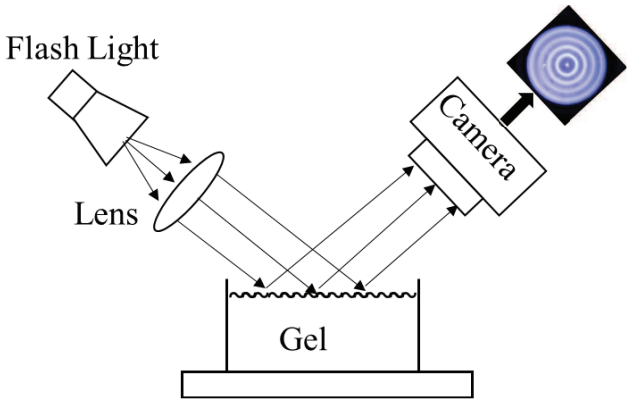

Figure 5.2: Optical system consists of a collimated light reflecting off the gel surface and collected by camera

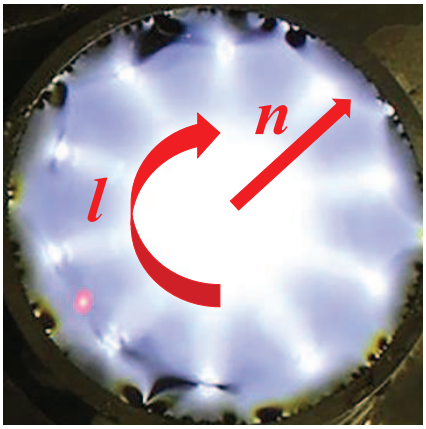

Figure 5.3: A typical radial-azimuthal wave pattern with radial n and azimuthal l mode

$\eta = J_n(lr)\cos(n\theta)$. The maximum value for the cross-correlation coefficient corresponds to the observed wave pattern. Because of the existence of a phase difference in the azimuthal direction between the wave pattern and the test pattern, the test pattern is rotated about its center by 1° in each computation and compute the associated cross correlation. There are 360 cross correlations calculated for a fixed n and l combination and the maximum within the results corresponds to the zero phase difference condition between the two images. The computational routine is illustrated in Fig. 5.4; 2-D cross correlations between three wave pattern images and the test pattern matrix with

$n, l = 1, 2, 3, 4$ are computed. The maximum cross-correlation coefficient for the first

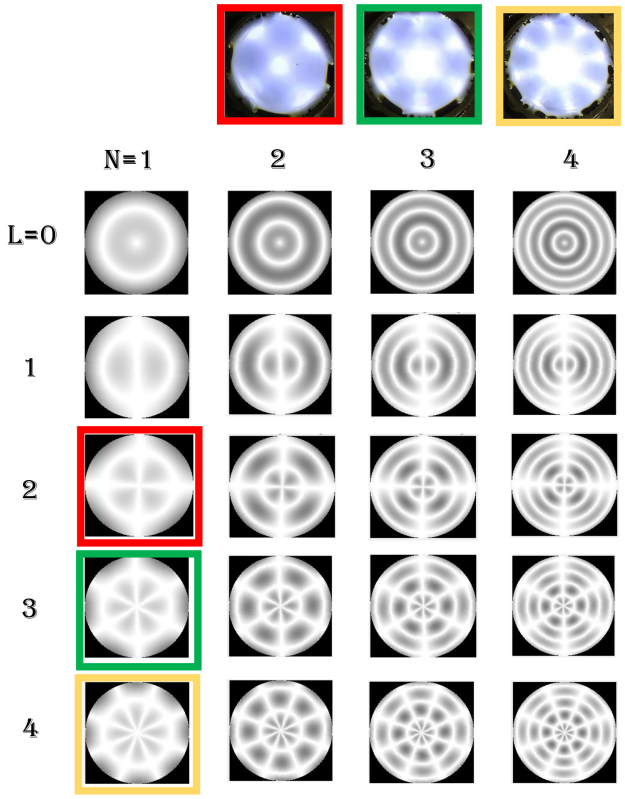

Figure 5.4: 2-D cross correlations between experiment and Bessel function surface modes

pattern corresponds to the $(n = 1, l = 2)$ mode, for the second $(1, 3)$, and for the third $(1, 4)$.

Two types of materials are studied; 1) glycerol/water mixtures and 2) agarose gels. Glycerol/water mixture is a type of Newtonian fluid (with $E = 0$) whose viscosity is tunable by changing the volume ratio between glycerol and water. Three different viscosities $\mu = 0.96, 2.3, 4.2$ mPa·s are explored in the experiments by fully mixing the glycerol with doubly distilled water. The agarose gels are prepared by dissolving agarose powder Sigma Aldrich Type VI-A in doubly distilled water. The mixture is kept in 90°C for an hour to ensure the powder is fully dissolved and then poured into the circular container. The mixture is allowed to be cooled at room temperature for 4 hours and completely covered to avoid evaporation before starting the experiment. I investigate the agarose

gels with a range of shear modulus $G = 0.4 - 12.2$Pa, which corresponds to the powder concentration $\phi = 0.045 - 0.108$%w. The agarose gels in our experiments exhibit a constant storage modulus over a range of frequencies used in experiment, which is one order magnitude larger than the loss modulus G'' . Therefore, the gels are concluded behave as linear elastic solids characterized only by a shear modulus $G = G'$ within a range of frequencies.

5.3 Experimental results

First, the Faraday wave patterns are studied on water. The first 50 Faraday waves mode shapes are obtained by performing a frequency sweep with $f_d = 7.1 - 46.8$Hz. The corresponding 50 mode shapes are shown in Fig. 5.5 with the associated observed frequency range. All patterns exhibit sub-harmonic response $f_o = 0.5 f_d$. The range of frequencies can be associated with the bandwidth of this particular mode and the resonance frequency can be associated with the minimum value of the tongue. Fig. 5.6 is a plot of the threshold amplitude versus driving frequency for the 17 threshold tongues obtained within the frequency range from $f_d = 10.2 - 28.1$Hz. 5 complete instability tongues are obtained in the range of driving frequencies $f_d = 10.2 - 16.0$Hz, but for higher frequencies incomplete tongues are observed, e.g., $(2,2)$, $(1,5)$, $(2,3)$, $(1,6)$, $(3,1)$, $(2,5)$, $(3,0)$, $(1,8)$, $(4,1)$. The exceptions are $(2,0)$,$(2,4)$, $(3,2)$, $(2,0)$, $(3,3)$, $(2,6)$ for which a resonance frequency can be identified. This observation indicates that very complicated mode competition exists in higher f_d. Mode (1,2) is the first mode plotted in Fig. 5.6 and is located a relatively large distance away from the lower frequency (1,1) mode in frequency space. Since the (1,2) mode faces the least mode competition, this mode is targeted in the investigations of the role of viscosity and elasticity on the shape of the instability tongues.

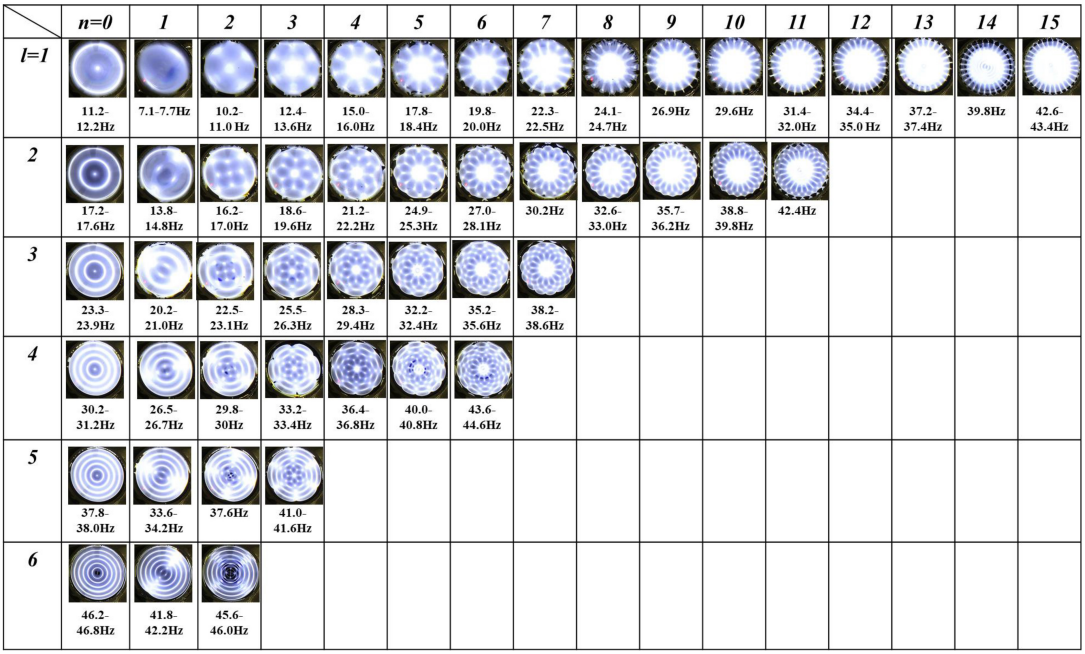

Figure 5.5: Mode table defined by the mode number pair (n, l) of observed Faraday waves. The frequency range over which that mode was excited is given below the mode shape.

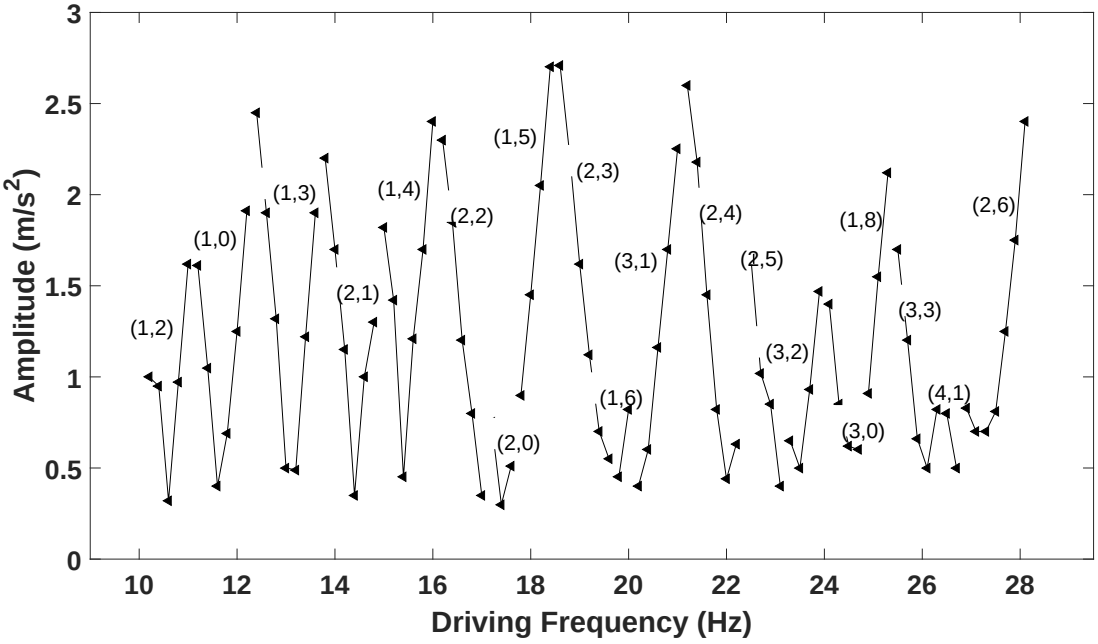

Figure 5.6: Faraday waves tongues on water in the amplitude-driving frequency space

Glycerol/water ratio	0:1	1:3	5:8
Surface tension (N/m)	0.072	0.068	0.062
Viscosity (mPa·s)	0.96	2.3	4.2
Density (kg/m^3)	1000	1070	1109
Ohnesorge number **Oh**	0.000605	0.00144	0.00271

Table 5.1: Material properties of the glycerol/water mixture ratios explored in this work.

5.3.1 Viscous effect in Faraday instability tongues

Glycerol/water mixtures are used to investigate the role of viscosity on the shape of the instability tongue. Here viscosity works as the dissipation while surface tension works as restorative force. Fig. 5.7 is a plot of the threshold amplitude against driving frequency for wave modes (1,2), (1,3) and (1,4) whose shapes are shown in Fig. 5.8. The material properties and the Ohnesorge number $\mathbf{Oh} = \mu/\sqrt{\rho R\sigma}$ of each material are listed in Table. 5.1. Since the densities for the materials are within a narrow range, **Oh** here represents the interplay of viscosity and surface tension in the experiments. For fixed mode number, the threshold amplitude increases with **Oh**, whereas the natural frequency is shifted to lower regime for increasing **Oh**. This follows the previous understanding of the role of of viscosity (dissipation) and surface tension (restorative force) in gel drops and edge waves discussed in Chapters 3 and 4. The fact that the threshold amplitude increases with mode number indicates higher dissipation associated with more complex surface patterns that delays the onset of Faraday waves in these higher modes.

5.3.2 Elastic effect in Faraday instability tongues

Elastic effects are investigated on agarose gels. The modes (1,2), (1,0), (1,3), (2,1), (1,4), (2,2), (2,0) are obtained on a gel with shear modulus $G = 3.9$ Pa within the driving frequency range $f_d = 9.8 - 19.2$Hz and plot the instability tongues in Fig. 5.9. Here there are five complete instability tongues for modes (1,2), (1,0), (1,3), (2,1), (2,2), from which the resonance frequency f_n and threshold amplitude a_n can be extracted. Values for f_n and a_n are listed in Table. 5.2 and contrasted with the associated values for water. It shows a consistent trend of increasing threshold amplitude with frequency and a dramatic difference in threshold amplitude for even small values of elasticity. Notably, the threshold amplitudes for the five modes on gels are almost 10 times larger than that on water. The order of the appearance of each mode follows the sequence of that on water

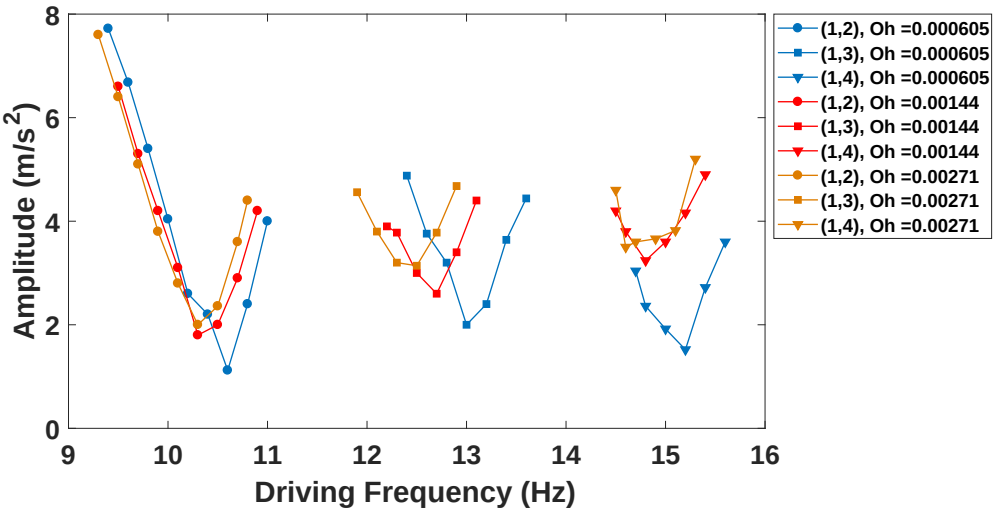

Figure 5.7: Faraday wave tongues on glycerol/water mixtures showing (1,2), (1,3), and (1,4) mode, as they depend upon Ohnesorge number

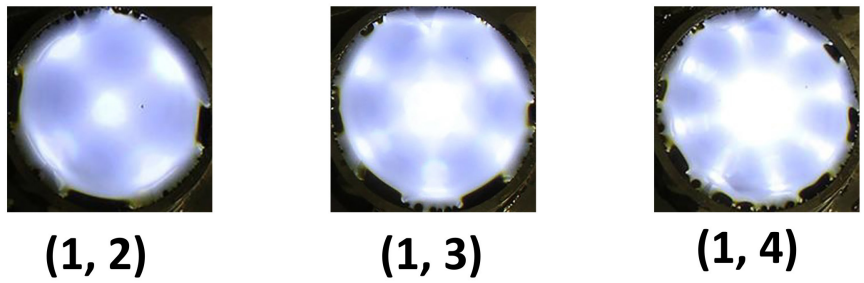

Figure 5.8: Typical (1,2), (1,3), (1,4) modes

although incomplete tongues are observed for modes (1,4),(2,0). It is noted there is a tendency that the threshold amplitude for gels is markedly higher than that for glycerol/water mixtures (cf. Fig. 5.7).

The role of elasticity is systematically studied on the instability tongue of (1,2) mode over the range of shear modulus $G = 0.4 - 12.2$ Pa. The plot of the threshold amplitude versus the driving frequency is shown in Fig. 5.11. The threshold tongue for water is added to Fig. 5.11 for a zero elasticity reference. For agarose gels, both elasticity and surface tension work as the restorative force to the system. Note the shift of threshold tongues on gels are much more complicated than that on viscous liquids. For ultra-soft gels, $G = 0.4 - 3.1$Pa, the resonance frequency is slightly shifted to lower frequency compared to that of water. This suggests surface tension decreases in

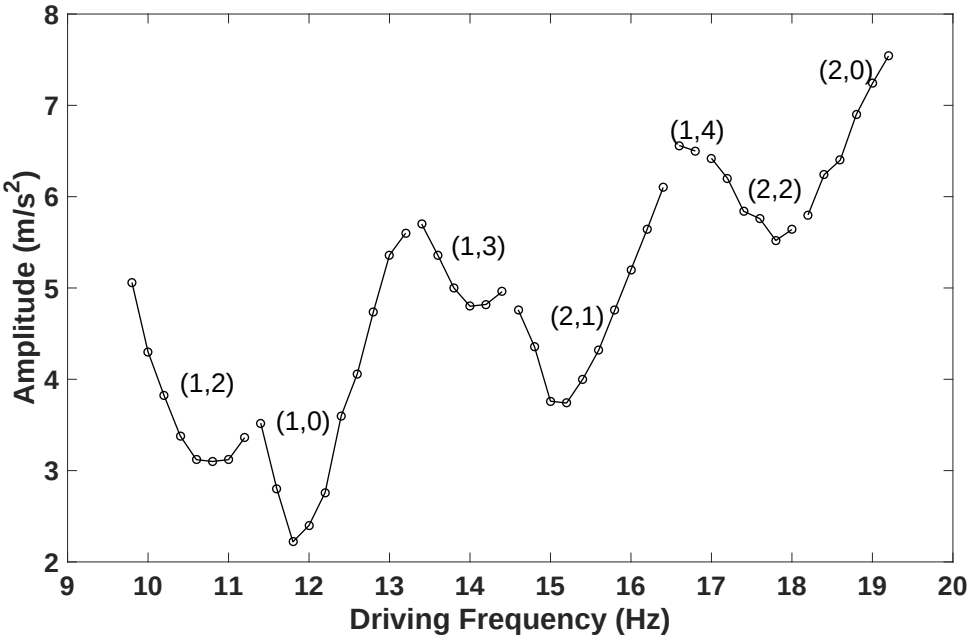

Figure 5.9: Faraday waves tongues for a gel with G =3.9 Pa in the amplitude-driving frequency space

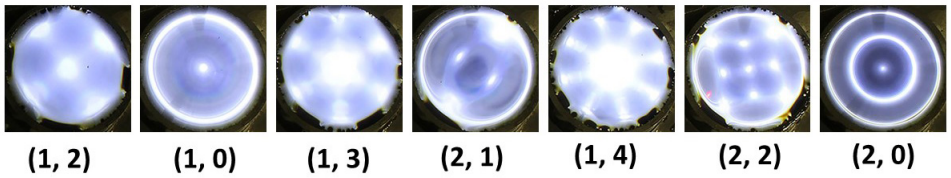

Figure 5.10: Typical (1,2), (1,0), (1,3), (2,1), (1,4), (2,2), (2,0) modes on gel with $G = 3.9$ Pa.

this range and the interplay gives rise to a smaller overall restorative force on ultrasoft gels than that on water and thus decreases the resonance frequency. It is noted that this surface tension decrease hypothesis follows the result of surface tension measurements on gels in Chapter 2. For larger shear modulus $G = 3.5 - 12.2$Pa, the resonance frequency increases monotonically with G. The threshold amplitude increases with G and quickly plateaus to a constant value for $G > 3.5$ Pa. Further theoretical analysis is needed to full understand the role of elasticity in Faraday waves.

mode number	(1,2)	(1,0)	(1,3)	(2,1)	(2,2)
$a_n(m/s^2)$ /water	0.32	0.4	0.49	0.35	0.35
$a_n(m/s^2)$ /gel	3.1	2.22	4.8	3.75	5.52
f_n (Hz) /water	10.6	11.6	13.2	14.4	17.0
f_n (Hz) /gel	10.8	11.8	14.0	15.2	17.8

Table 5.2: Resonance frequency f_n and amplitude a_n for the first five modes for water and a gel with $G = 3.9$ Pa.

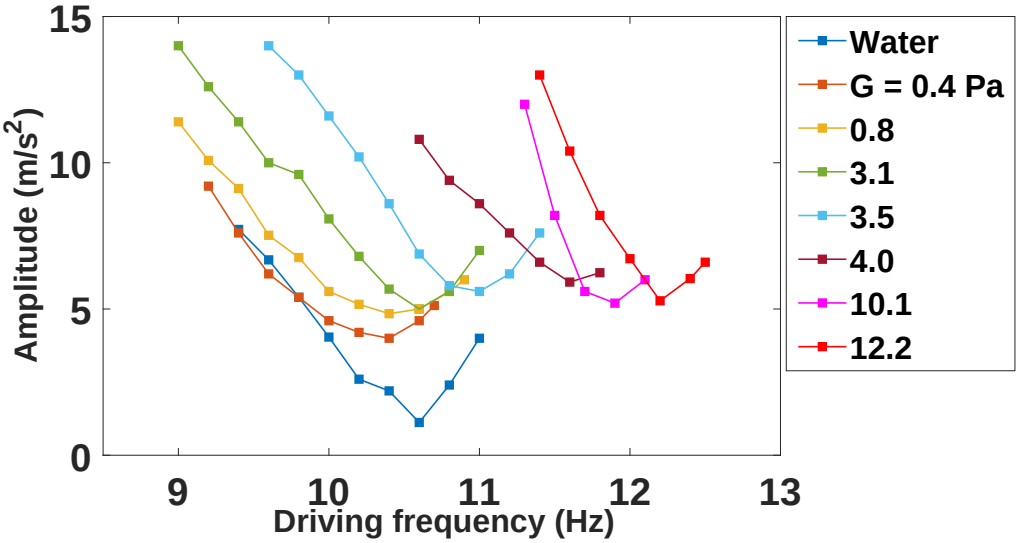

Figure 5.11: Instability tongue for the (1,2) mode as it depends upon the shear modulus G

5.4 Discussion

Experiments have been conducted to characterize the effect of material properties in changing the shape of Faraday instability tongues and highlight the role of elasticity in shifting the resonance frequency of Faraday wave mode by exploring gels over a range of shear modulus. To our knowledge this is the first observation of Faraday wave instability tongues on gels. For the ultra-soft gels ($G < 5$ Pa), elasticity also exhibits a relatively strong effect in increasing the threshold amplitude and a complicated interplay between capillarity and elasticity exists in this regime observing the non-monotonic shift of resonance frequency with shear modulus. In comparison, in liquids, viscosity shows a consistent damping effect in increasing the threshold amplitude and decreasing the resonance frequency. The experiments emphasizes the role of surface tension and elasticity as the restorative force and viscosity as dissipation to the system. Further theoretical analysis is needed to

quantified the elasticity impact in the restorative force and dissipation in the onset mechanism for Faraday waves.

Henderson and Miles [53] reported the corner effect of a rectangular tank can significantly increased the damping rates of Faraday waves on liquids and which is not observed on a circular container. It is worthwhile to study the Faraday waves on gels in a rectangular tank and explore the higher dissipation effect in reconfiguring the pattern formation on gels and changing the shape of Faraday instability tongues. The combination of Faraday wave studies in a circular tank and rectangualr tank can reveal more details about potential contact-line dynamics in gels. It has also been noted that for viscoelastic materials, there is a relaxation time scale t_p and it has been shown that harmonic Faraday waves can be observed when the time scale of the forcing frequency approaches $1/t_p$[112]. The harmonic response has not been observed in this study since t_p in gels is beyond the driving frequency range in this experiment, but it is definitely an important part in future works to study the instability tongues on harmonic Faraday waves.

The agarose gels used in the experiments exhibit constant rheological behaviors over a wide range of driving frequencies. It is meaningful to study the pattern formation of Faraday waves on other gels with complicated frequency dependent rheological properties. It is expected that the frequency dependent viscosity and elasticity can change the shape of Faraday instability tongue in a completely new manner from previous experiments in literature featuring multiple resonances for one mode and odd tongue shapes. In addition, it is noted many new interesting phenomena in particle separations have been observed on non-Newtonian fluids such as xantham gum and polyacrylamide solutions whose viscosity can change with external forcing shear rate[82, 64]. For strong shear thinning and shear thickening materials, it is possible to obtain some new pattern formation phenomena by exciting Faraday waves in higher frequency regime. These hypotheses should be validated through further experimental and theoretical studies on this area.

Lastly, it is noted that an interesting observation of mode mixing of edge waves and Faraday waves in the experiments with water as working material. Recall in Chapter 4 that the protocol of generating the edge waves has been demonstrated by slightly under filling the tank and thus leaving a meniscus at the pinned edge, which will excite edge waves propagating inward. In contrast, to excite pure Faraday waves, the container is perfectly filled to the edge to eliminate the meniscus. By slightly underfilling the tank, mixing mode patterns will be observed when the forcing amplitude and driving frequency are in the Faraday wave regime. In Fig. 5.12 (a), the evolution of a mixing mode

pattern is exhibited from pure edge waves at a fixed frequency by increasing the forcing amplitude. The first picture displays the pure edge waves excited when the forcing amplitude is below the Faraday wave threshold and the second picture displays the emergence of mixing mode by setting the forcing amplitude near threshold. The final three images illustrate the evolution of the mixing mode with increasing forcing amplitude Fig. 5.12 (b) illustrates a number of mode mixing pairs and the corresponding frequency. These beautiful images of pattern formation exhibit complex dynamics dynamics and further theoretical analysis is needed to understand the complex interplay between the two types of waves.

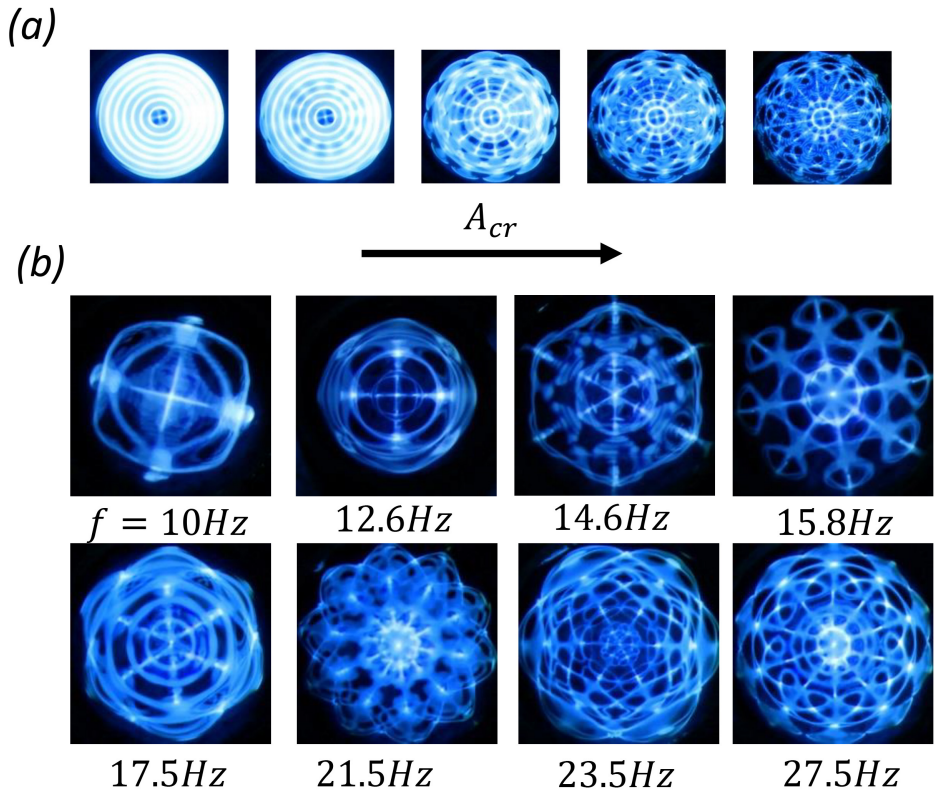

Figure 5.12: Mode mixing. (a) Evolution of a pure edge wave into a mixed mode of edge wave and Faraday wave upon increasing forcing amplitude; (b) Various mode mixing patterns have been observed at varying driving frequencies.

Chapter 6

Conclusion

In this dissertation, the elastocapillary phenomena on soft gels have been studied from both experimental and theoretical perspectives. A number of first experimental observations are reported including i) gel drop oscillations and ii) Faraday waves on gels. The elastocapillary transition has been successfully characterized through dispersion relationships for both planar surfaces and spherical droplets, of which capillary waves and elastic waves naturally arise as the two limiting cases. Periodic forcing is shown to give rise to pattern formation phenomena which are characterized i) the frequency response of harmonic edge waves and ii) the instability tongues for sub-harmonic Faraday waves, as it depends upon the elasticity for soft hydrogels. There is a complex interplay between capillarity, elasticity, and viscosity in soft hydrogels and a diagnostic technique has notably been developed to measure each of these material properties using the surface waves dynamics.

Rayleigh-Taylor instability (RTI) has been observed on the free surface of gels when the elastogravity length $L_g = \rho g/G$ is smaller than the height of the gel h[108]. This highlights the interplay between elasticity and gravity in determining the pattern formation on ultrasoft gels ($G \leq$ 40Pa) in low wave number regime. In Chapter 2, the role of gravity in the dispersion relationship of elastocapillary waves has been revealed when $G \to 0$. The proposed closed-form dispersion relationship in Eq. (2.12) can be used to study RTI on gels by predicting the wave number k for a given G by reserving the orientation of the gravity.

In Chapter 3, an empirical dispersion relationship is proposed for oscillating gel droplets from a 1-D damped driven oscillator model by idealizing the restorative force of surface tension and elasticity as spring constants in parallel, and viscous dissipation as a damping constant. This model

neglects the coupling between elasticity and surface tension that would appear naturally in linear elasticity model. Furthermore, to include viscous effects would require the introduction of a full viscoelastic model with characteristic viscous relaxation time scale through the Deborah number. This is particularly needed for gels with more complex rheology. In addition, the aspect ratio of the levitated gel droplets deviate from sphericity in the drop levitation experiments, even through gel drops have been made spherical by using the neutral buoyancy approach. This is due to the acoustic pressure needed to levitate the drop. The model does not account for this deviation in sphericity. A rigorous theoretical model which accounts for these factors is needed for further analysis.

The radius of the gel droplets explored in the experiments was in a narrow range 1.2mm$<$ r $<$ 1.6mm and this is primarily due to the technique for making large droplets (surface tension tend to pinch off the pendant droplet attached on the nozzle). The narrow radius range limits the technique for simultaneously measuring the surface tension σ and shear modulus G from Eq. 3.9. The shear modulus G had to be measured separately in a rheometer in this study, whereas if the drop radius could be varied over a large range, G should be measured independently with the approach. This should be the focus of future work.

In addition, the higher resonance modes $n > 2$ for gel droplets were not explored, but the study of higher order resonance modes can be advantageous, e.g., the higher wave number can weaken the non-sphericity geometry effect and might display more disspation within a gel droplet oscillation. Also, the transition from underdamped to overdamped oscillations in these modes can be useful in characterizing the dissipation in the system. However, it is challenging with the current laser light detection approach to determine the resonance for higher modes, since the deformations for modes $n > 2$ are much more complicated and do not follow the maximum projected area as mode $n = 2$ does [146]. This would mostly likely need to be done via high-speed imaging.

In Chapter 4, multiple $n = 2$ modes are observed for edge waves on gels with $G > 3.6$ Pa. In Chapter 5, multiple (1,2) modes are obtained for $G > 12.2$ Pa and the different (1,2) modes are separated by (1,0) mode in the driving frequency space. These experimental observations indicate nonlinear dispersion relationships exist on gels. The nonlinear dispersive behavior has been reported on deep-water gravity waves, which is known as the Benjamin-Feir instability (BFI) [11]. The BFI describes a uniform train of oscillatory waves in moderate amplitude loses energy to a small perturbation and evolves into a narrow-banded spectrum of waves. The wave trains are stable when the dissipation of the wave system stabilizes this narrow-banded surface waves by suppressing the

growth of further nonlinear perturbations and spreads energy from this initially narrow bandwidth to a broader bandwidth [134, 20]. In Chapter 3, the viscosities on gels are shown to be about thirty times larger than that on water over a wide range of shear modulus, which can provide the larger dissipation for stabilizing the BFI and preventing the further nonlinear wave interactions. However, there is no conclusion about the mechanism of the nonlinear dispersion relationship on gels yet. This should be pursued further in future studies.

Lastly, agarose hydrogels have been purposefully used in the experiments, because it exhibits a constant rheological behavior over a wide range of driving frequency and the competition between surface tension and elasticity is studied in a relatively simple material. More complex materials exhibit a frequency dependent material properties such that the complex modulus $G = G' + iG''$ depends on the frequency in a complex functional way. The rheological measurement protocol developed in Chapter 3 is not able to determine G and μ of frequency dependent materials. It is noted that non-Newtonian viscoelastic materials such as xanthan gum (XG) solution, Polyacrylamide (PAA) solution, and Hyaluronic acid (HA) solution have exhibited enormous advantages in particle separation in microchannels, because the additional hydrodynamics force induced by elasticity and by side wall from shear thinning effect[82, 81]. In addition, harmonic Faraday waves were generated on the PAA solution and gave rise to new pattern formation phenomena not yet observed in Newtonian fluids[159]. The frequency dependent material properties have the potential to influence the pattern formation in a similar manner as the non-Newtonian fluids does since inherent material induced elastic and viscous force difference over a range of frequencies can add more complexities to the system. This would be explored in future studies.

Appendices

Appendix A

The dispersion relationship Eq. (4.2) which presented in Chapter 4 is derived in this appendix.

Consider a fluid with interface at $z = 0$, endowed with surface tension σ, in a cylindrical container with radius R that extends to infinity in negative z direction. The flow is assumed to be irrotational $\mathbf{v} = \nabla\phi$ where ϕ is the velocity potential which satisfies Laplace's equation

$$\nabla^2\phi = 0. \tag{1}$$

The no-penetration condition is enforced on the lateral boundary $r = R$,

$$\frac{\partial\phi}{\partial r} = 0, \tag{2}$$

and a kinematic condition at the free surface $z = 0$,

$$\frac{\partial\phi}{\partial z} = \frac{\partial\eta}{\partial t}, \tag{3}$$

which relates ϕ to the linearized interface disturbance η. The jump in normal stress across the interface is related to the curvature there via the Young-Laplace equation,

$$p - 2\mu\frac{\partial^2\phi}{\partial z^2} = -\frac{\sigma}{R^2}\left(\frac{d^2\eta}{dr^2} + \frac{1}{r}\frac{d\eta}{dr}\right). \tag{4}$$

Note that the viscosity μ has been kept in the boundary condition and this is sometimes referred to as viscous potential flow. Elasticity G is introduced through the complex viscosity $\mu \to \mu + G/i\omega$,

where ω is the oscillation frequency and this gives

$$p - 2\mu\frac{\partial^2\phi}{\partial z^2} - \frac{2G}{i\omega}\frac{\partial^2\phi}{\partial z^2} = -\frac{\sigma}{R^2}\left(\frac{d^2\eta}{dr^2} + \frac{1}{r}\frac{d\eta}{dr}\right). \tag{5}$$

Lastly, the linearized Bernoulli equation is written as

$$\rho\frac{\partial\phi}{\partial t} = -p - \rho g\eta. \tag{6}$$

Normal modes are assumed,

$$\eta(r,t) = AJ_0(kr)\mathrm{e}^{i\omega t},\ \phi(r,z,t) = BJ_0(kr)\mathrm{e}^{-kz}\mathrm{e}^{i\omega t}, \tag{7}$$

where J_0 is the Bessel function and k the wavenumber, and applied to the governing Equations (1,2,3,5,6). Lengths are scaled by R, time by the capillary time scale $\sqrt{\rho R^3/\sigma}$, and this gives rise to the following dispersion relationship

$$\lambda = i\mathrm{Oh}k^2 \pm \sqrt{\mathrm{Bo}k + k^3 + 2k^2\mathrm{Ec} - \mathrm{Oh}^2k^4} \tag{8}$$

where $\lambda = \sqrt{\rho R^3\omega^2/\sigma}$ is the scaled frequency , $\mathrm{Oh} = \mu/\sqrt{\rho R\sigma}$ the Ohnesorge number, $\mathrm{Bo} = \rho R^2 g/\sigma$ the Bond number, and $\mathrm{Ec} = GR/\sigma$ the elastocapillary number. The wavenumber k is determined by the boundary conditions at the sidewall $J_0'(k) = 0$.

Bibliography

[1] A.W. Adamson. *Physical Chemistry of Surfaces*. John Wiley & Sons, New York, NY, 1990.

[2] B. Andreotti, O. Bäumchen, F. Boulogne, K. E. Daniels, E. R. Dufresne, H. Perrin, T. Salez, J. H. Snoeijer, and R. W. Style. Solid capillarity: when and how does surface tension deform soft solids? *Soft Matter*, 12(12):2993–2996, 2016.

[3] B. Andreotti and J. H. Snoeijer. Soft wetting and the shuttleworth effect, at the crossroads between thermodynamics and mechanics. *EPL (Europhysics Letters)*, 113(6):66001, 2016.

[4] F. Ardhuin, L. Marié, N. Rascle, P. Forget, and A. Roland. Observation and estimation of lagrangian, stokes, and eulerian currents induced by wind and waves at the sea surface. *Journal of Physical Oceanography*, 39(11):2820–2838, 2009.

[5] P. Ball. Forging patterns and making waves from biology to geology: a commentary on turing (1952)the chemical basis of morphogenesis. *Philosophical Transactions of the Royal Society B: Biological Sciences*, 370(1666):20140218, 2015.

[6] P. Ballesta, M. P. Lettinga, and S. Manneville. Interplay between a hydrodynamic instability and a phase transition: the faraday instability in dispersions of rodlike colloids. *Soft Matter*, 7(24):11440–11446, 2011.

[7] P. Ballesta and S. Manneville. Signature of elasticity in the Faraday instability. *Physical Review E*, 71:026308, 2005.

[8] S.I. Bastrukov. Low-frequency elastic response of a spherical particle. *Physical Review E*, 49(4):3166, 1994.

[9] W. Batson, F. Zoueshtiagh, and R. Narayanan. The faraday threshold in small cylinders and the sidewall non-ideality. *Journal of Fluid Mechanics*, 729:496–523, 2013.

[10] J. Bechhoefer, V. Ego, S. Manneville, and B. Johnson. An experimental study of the onset of parametrically pumped surface waves in viscous fluids. *Journal of Fluid Mechanics*, 288:325–350, 1995.

[11] T.B. Benjamin and J.E. Feir. The disintegration of wave trains on deep water. *Journal of Fluid Mechanics*, 27(3):417–430, 1967.

[12] T.B. Benjamin and F.J. Ursell. The stability of the plane free surface of a liquid in vertical periodic motion. *Proceedings of the Royal Society of London. Series A. Mathematical and Physical Sciences*, 225(1163):505–515, 1954.

[13] L. E. Bertassoni, M. Cecconi, V. Manoharan, M. Nikkhah, J. Hjortnaes, A. L. Cristino, G. Barabaschi, D. Demarchi, M. R. Dokmeci, Y. Yang, et al. Hydrogel bioprinted microchannel networks for vascularization of tissue engineering constructs. *Lab on a Chip*, 14(13):2202–2211, 2014.

[14] D. Binks and W. van de Water. Nonlinear pattern formation of faraday waves. *Physical Review Letters*, 78(21):4043, 1997.

[15] J.B. Bostwick, M. Shearer, and K.E. Daniels. Elastocapillary deformations on partially-wetting substrates: rival contact-line models. *Soft Matter*, 10(37):7361–7369, 2014.

[16] J.B. Bostwick and P.H. Steen. Coupled oscillations of deformable spherical-cap droplets. part 2. viscous motions. *Journal of Fluid Mechanics.*, 714:336–360, 2013.

[17] J.B. Bostwick and P.H. Steen. Stability of constrained capillary surfaces. *Annual Review of Fluid Mechanics.*, 47:539–568, 2015.

[18] J.B. Bostwick and P.H Steen. Static rivulet instabilities: varicose and sinuous modes. *Journal of Fluid Mechanics*, 837:819–838, 2018.

[19] O. Breslouer. Rayleigh-plateau instability: falling jet. *Project Report*, 2010.

[20] T.J. Bridges and F. Dias. Enhancement of the benjamin-feir instability with dissipation. *Physics of fluids*, 19(10):104104, 2007.

[21] J. Brum, S. Catheline, N. Benech, and C. Negreira. Shear elasticity estimation from surface wave: the time reversal approach. *The Journal of the Acoustical Society of America*, 124(6):3377–3380, 2008.

[22] C. Cabeza and M. Rosen. Complexisty in Faraday experiment with viscoelastic fluid. *International Journal of Bufurcation and Chaos*, 17:1599–1607, 2007.

[23] K.M. Case and W.C. Parkinson. Damping of surface waves in an incompressible liquid. *Journal of Fluid Mechanics*, 2(2):172–184, 1957.

[24] J.R. Castrejon-Pita, W.R.S Baxter, J. Morgan, S. Temple, G.D. Martin, and I.M. Hutchings. Future, opportunities and challenges of inkjet technologies. *Atomization and Sprays*, 23(6), 2013.

[25] A. Chakrabarti. *Elastocapillary Phenomena in Soft Elastic Solids.* PhD thesis, Lehigh University, 2017.

[26] A. Chakrabarti and M.K. Chaudhury. Direct measurement of the surface tension of a soft elastic hydrogel: exploration of elastocapillary instability in adhesion. *Langmuir*, 29(23):6926–6935, 2013.

[27] Aditi Chakrabarti and Manoj K Chaudhury. Vibrations of sessile drops of soft hydrogels. *Extreme Mechanics Letters*, 1:47–53, 2014.

[28] C. Chang, J.B. Bostwick, S. Daniel, and P.H. Steen. Dynamics of sessile drops. part 2. experiment. *Journal of Fluid Mechanics*, 768:442–467, 2015.

[29] P. Choi, E. Jyounouti, K. Yamamoto, and K. Takagi. Visualization of shear waves radiated from pseudocapillary mode on agarose gel by stroboscopic photoelasticity technique. *Japanese Journal of Applied Physics*, 40(5S):3526, 2001.

[30] P-K Choi, E. Jyounouti, K. Yuuki, and Y. Onodera. Experimental observation of pseudocapillary and rayleigh modes on soft gels. *The Journal of the Acoustical Society of America*, 106(3):1591–1593, 1999.

[31] B. Christiansen, M.T. Levinsen, et al. Ordered capillary-wave states: quasicrystals, hexagons, and radial waves. *Physical Review Letters*, 68(14):2157, 1992.

[32] M.C. Cross and P.C. Hohenberg. Pattern formation outside of equilibrium. *Reviews of Modern Physics*, 65(3):851, 1993.

[33] S.H. Davis. Moving contact lines and rivulet instabilities. part 1. the static rivulet. *Journal of Fluid Mechanic*, 98:225–242, 1980.

[34] L. Deike, S. Popinet, and W.K. Melville. Capillary effects on wave breaking. *Journal of Fluid Mechanics*, 769:541–569, 2015.

[35] U. Demirci and G. Montesano. Single cell epitaxy by acoustic picolitre droplets. *Lab on a Chip*, 7(9):1139–1145, 2007.

[36] S. Douady. Experimental study of the faraday instability. *Journal of Fluid Mechanics*, 221:383–409, 1990.

[37] S. Douady and S. Fauve. Pattern selection in faraday instability. *EPL (Europhysics Letters)*, 6(3):221, 1988.

[38] W. S. Edwards and S. Fauve. Parametrically excited quasicrystalline surface waves. *Physical Review E*, 47(2):R788, 1993.

[39] A.C. Eringen, E.S. Suhubi, and C.C. Chao. Elastodynamics, vol. ii, linear theory. *Journal of Applied Mechanics*, 45, 1978.

[40] R. Fan, M. Piou, E. Darling, D. Cormier, J. Sun, and J. Wan. Bio-printing cell-laden matrigel–agarose constructs. *Journal of Biomaterials Applications*, 31(5):684–692, 2016.

[41] M. Faraday. On a peculiar class of acoustical figures; and on certain forms assumed by groups of particles upon vibrating elastic surfaces. *Philosophical transactions of the Royal Society of London*, 121:299–340, 1831.

[42] M. Faraday. On the forms and states assumed by fluids in contact with vibrating elastic surfaces. *Philosophical Transactions of the Royal Society*, 121:39–346, 1831.

[43] S. Fauve, K. Kumar, C. Laroche, D. Beysens, and Y. Garrabos. Parametric instability of a liquid-vapor interface close to the critical point. *Physical review letters*, 68(21):3160, 1992.

[44] N.E. Fedorovich, J. Alblas, J.R. de Wijn, W.E. Hennink, A.J. Verbout, and W.J.A. Dhert. Hydrogels as extracellular matrices for skeletal tissue engineering: state-of-the-art and novel application in organ printing. *Tissue Engineering*, 13(8):1905–1925, 2007.

[45] S. Fredericks and J. R. Saylor. Experimental study of drop shape and wake effects on particle scavenging for non-evaporating drops using ultrasonic levitation. *Journal of Aerosol Science.*, 127:1 – 17, 2019.

[46] S. Fredericks and J.R. Saylor. Experimental study of drop shape and wake effects on particle scavenging for non-evaporating drops using ultrasonic levitation. *Journal of Aerosol Science*, 127:1–17, 2019.

[47] D.C. Fritts and M. J. Alexander. Gravity wave dynamics and effects in the middle atmosphere. *Reviews of Geophysics*, 41(1), 2003.

[48] G. L. Gaines Jr. *Insoluble Monolayers at Liquid-Gas Interfaces*. John Wiley & Sons, New York, NY, 1966.

[49] J.P. Gollub and J.S. Langer. Pattern formation in nonequilibrium physics. *Reviews of Modern Physics*, 71(2):S396, 1999.

[50] M. Grzelka, J.B. Bostwick, and K.E. Daniels. Capillary fracture of ultrasoft gels: variability and delayed nucleation. *Soft Matter*, 13(16):2962–2966, 2017.

[51] H. Gudapati, M. Dey, and I. Ozbolat. A comprehensive review on droplet-based bioprinting: Past, present and future. *Biomaterials*, 102:20–42, 2016.

[52] J.L. Harden, H. Pleiner, and P.A. Pincus. Hydrodynamic surface modes on concentrated polymer solutions and gels. *The Journal of Chemical Physics*, 94(7):5208–5221, 1991.

[53] D.M. Henderson and J.W. Miles. Single-mode faraday waves in small cylinders. *Journal of Fluid Mechanics*, 213:95–109, 1990.

[54] M.L. Henle and A.J. Levine. Capillary wave dynamics on supported viscoelastic films: single and double layers. *Physical Review E*, 75(2):021604, 2007.

[55] S. Hitchman, K. van Wijk, and Z. Davidson. Monitoring attenuation and the elastic properties of an apple with laser ultrasound. *Postharvest Biology and Technology*, 121:71–77, 2016.

[56] LM Hocking. The damping of capillary–gravity waves at a rigid boundary. *Journal of Fluid Mechanics*, 179:253–266, 1987.

[57] V. A. Hosseinzadeh, C. Brugnara, and R. G. Holt. Shape oscillations of single blood drops: applications to human blood and sickle cell disease. *Scientific Reports*, 8:16794, 2018.

[58] V. A. Hosseinzadeh and R. G. Holt. Finite amplitude effects on drop levitation for material properties measurement. *Journal of Applied Physics.*, 121:174502, 2017.

[59] V.A. Hosseinzadeh, C. Brugnara, and R.G. Holt. Shape oscillations of single blood drops: applications to human blood and sickle cell disease. *Scientific Reports*, 8(1):1–8, 2018.

[60] C.-J. Hsu and R. E. Apfel. A technique for measuring interfacial tension by quadrupole oscillation of drops. *Journal of Colloid and Interface Science.*, 107(2):467–476, 1985.

[61] C. Hui and A. Jagota. Deformation near a liquid contact line on an elastic substrate. *Proceedings of the Royal Society A: Mathematical, Physical and Engineering Sciences*, 470(2167):20140085, 2014.

[62] T. Ikeda, P. Choi, T. Ishii, I. Arai, and M. Osawa. Firmness evaluation of watermelon flesh by using surface elastic waves. *Journal of Food Engineering*, 160:28–33, 2015.

[63] U. Irion, J. Adams, C. Chang, and D. St Johnston. Miranda couples oskar mrna/staufen complexes to the bicoid mrna localization pathway. *Developmental Biology*, 297(2):522–533, 2006.

[64] P.P. Jagdale, D. Li, X. Shao, J.B. Bostwick, and X. Xuan. Fluid rheological effects on the flow of polymer solutions in a contraction–expansion microchannel. *Micromachines*, 11(3):278, 2020.

[65] A. Javadi, J. Eggers, D. Bonn, M. Habibi, and N.M. Ribe. Delayed capillary breakup of falling viscous jets. *Physical Review Letters*, 110(14):144501, 2013.

[66] E. R. Jerison, Y. Xu, L.A. Wilen, and E.R. Dufresne. Deformation of an elastic substrate by a three-phase contact line. *Physical Review Letters.*, 106:186103, May 2011.

[67] S. Ji and M. Guvendiren. Recent advances in bioink design for 3d bioprinting of tissues and organs. *Frontiers in Bioengineering and Biotechnology*, 5, 2017.

[68] L. Jørgensen, M. Le Merrer, H. Delanoë-Ayari, and C. Barentin. Yield stress and elasticity influence on surface tension measurements. *Soft Matter*, 11(25):5111–5121, 2015.

[69] T. Kajiya, A. Daerr, T. Narita, L. Royon, F. Lequeux, and L. Limat. Advancing liquid contact line on visco-elastic gel substrates: stick-slip vs. continuous motions. *Soft Matter*, 9(2):454–461, 2013.

[70] J. Kappler and R.R. Netz. Multiple surface wave solutions on linear viscoelastic media. *EPL (Europhysics Letters)*, 112(1):19002, 2015.

[71] S. Karpitschka, S. Das, M. van Gorcum, H. Perrin, B. Andreotti, and J.H. Snoeijer. Droplets move over viscoelastic substrates by surfing a ridge. *Nature Communications*, 6:7891, 2015.

[72] S.V. Kiyashko, L.N. Korzinov, M.I. Rabinovich, and L.S. Tsimring. Rotating spirals in a faraday experiment. *Physical Review E*, 54(5):5037, 1996.

[73] A.H. Knoll and S.B. Carroll. Early animal evolution: emerging views from comparative biology and geology. *Science*, 284(5423):2129–2137, 1999.

[74] J. Kremer, A. Kilzer, and M. Petermann. Simultaneous measurement of surface tension and viscosity using freely decaying oscillations of acoustically levitated droplets. *Review of Scientific Instruments.*, 89:015109, 2018.

[75] A. Kudrolli and J.P. Gollub. Patterns and spatiotemporal chaos in parametrically forced surface waves: a systematic survey at large aspect ratio. *Physica D: Nonlinear Phenomena*, 97(1-3):133–154, 1996.

[76] K. Kumar and K.M.S. Bajaj. Competing patterns in the faraday experiment. *Physical Review E*, 52(5):R4606, 1995.

[77] K. Kumar and L.S. Tuckerman. Parametric instability of the interface between two fluids. *Journal of Fluid Mechanics*, 279:49–68, 1994.

[78] S. Kumar. Parametrically driven surface waves in viscoelastic liquids. *Physics of Fluids*, 11(8):1970–1981, 1999.

[79] H. Lamb. *Hydrodynamics*. Dover Inc., 1945.

[80] E.G. Lean and C.G. Powell. Nondestructive testing of thin films by harmonic generation of dispersive rayleigh waves. *Applied Physics Letters*, 19(9):356–359, 1971.

[81] A.M. Leshansky, A. Bransky, N. Korin, and U. Dinnar. Tunable nonlinear viscoelastic focusing in a microfluidic device. *Physical Review Letters*, 98(23):234501, 2007.

[82] D. Li, X. Shao, J.B. Bostwick, and X. Xuan. Particle separation in xanthan gum solutions. *Microfluidics and Nanofluidics*, 23(11):125, 2019.

[83] D. Linke, T. Riess, I.B. Autenrieth, A. Lupas, and V.A.J. Kempf. Trimeric autotransporter adhesins: variable structure, common function. *Trends in Microbiology*, 14(6):264–270, 2006.

[84] D. Livescu. Numerical simulations of two-fluid turbulent mixing at large density ratios and applications to the rayleigh–taylor instability. *Philosophical Transactions of the Royal Society A: Mathematical, Physical and Engineering Sciences*, 371(2003):20120185, 2013.

[85] R. Lord. Investigation of the character of the equilibrium of an incompressible heavy fluid of variable density. *Scientific Papers*, pages 200–207, 1900.

[86] L.A. Lubbers, J.H. Weijs, L. Botto, S. Das, B. Andreotti, and J.H. Snoeijer. Drops on soft solids: free energy and double transition of contact angles. *Journal of Fluid Mechanics*, 747, 2014.

[87] B.A. Luke and K.H. Stokoe II. Application of sasw method underwater. *Journal of Geotechnical and Geoenvironmental Engineering*, 124(6):523–531, 1998.

[88] T.M. MacRobert. *Spherical Harmonics*. Pergamon, New York, NY, 1967.

[89] F. Maderspacher and C. Nüsslein-Volhard. Formation of the adult pigment pattern in zebrafish requires leopard and obelix dependent cell interactions. *Development*, 130(15):3447–3457, 2003.

[90] A. Manduca, T.E. Oliphant, M.A. Dresner, J.L. Mahowald, S.A. Kruse, E. Amromin, J.P. Felmlee, J.F. Greenleaf, and R.L. Ehman. Magnetic resonance elastography: non-invasive mapping of tissue elasticity. *Medical Image Analysis*, 5(4):237–254, 2001.

[91] A. Marchand, S. Das, J.H. Snoeijer, and B. Andreotti. Contact angles on a soft solid: From youngs law to neumanns law. *Physical Review Letters*, 109(23):236101, 2012.

[92] P. L. Marston and R. E. Apfel. Acoustically forced shape oscillation of hydrocarbon drops levitated in water. *Journal of Colloid and Interface Science.*, 68:280–286, 1979.

[93] P. L. Marston and E. H. Trinh. Pseudo-extinction of light as a method for detecting acoustically induced shape oscillations of drops levitated in air. *The Journal of the Acoustical Society of America*, 77(S1):S20–S20, 1985.

[94] B. Masserey. *Ultrasonic surface crack characterization using Rayleigh waves*. PhD thesis, 2006.

[95] J. G. McDaniel and R. G. Holt. Measurement of aqueous foam rheology by acoustic levitation. *Physical Review E*, 61:2204, 2000.

[96] C.C. Mei and L.F. Liu. The damping of surface gravity waves in a bounded liquid. *Journal of Fluid Mechanics*, 59(2):239–256, 1973.

[97] H. Meinhardt. Models of biological pattern formation. *New York*, 1982.

[98] W.K. Melville. The role of surface-wave breaking in air-sea interaction. *Annual Review of Fluid Mechanics*, 28(1):279–321, 1996.

[99] W.K. Melville and P. Matusov. Distribution of breaking waves at the ocean surface. *Nature*, 417(6884):58–63, 2002.

[100] F.G. Mercier. Partially supervised oil-slick detection by sar imagery using kernel expansion. *IEEE Transactions on Geoscience and Remote Sensing*, 44(10):2839–2846, 2006.

[101] J. Miles and D. Henderson. Parametrically forced surface waves. *Annual Review of Fluid Mechanics*, 22(1):143–165, 1990.

[102] J.W. Miles. Surface-wave damping in closed basins. *Proceedings of the Royal Society of London. Series A. Mathematical and Physical Sciences*, 297(1451):459–475, 1967.

[103] Monroy. Surface hydrodynamics of viscoelastic fluids and soft solids: Surfing bulk rheology on capillary and rayleigh waves. *Advances in Colloid and Interface Science*, pages 4–22, 2017.

[104] F. Monroy and D. Langevin. Direct experimental observation of the crossover from capillary to elastic surface waves on soft gels. *Physical Review Letters*, 81(15):3167, 1998.

[105] S. Mora, M. Abkarian, H. Tabuteau, and Y. Pomeau. Surface instability of soft solids under strain. *Soft Matter*, 7(22):10612–10619, 2011.

[106] S. Mora, C. Maurini, T. Phou, J. Fromental, B. Audoly, and Y. Pomeau. Solid drops: large capillary deformations of immersed elastic rods. *Physical Review Letter.*, 111(11):114301, 2013.

[107] S. Mora, T. Phou, J. Fromental, L.M. Pismen, and Y. Pomeau. Capillarity driven instability of a soft solid. *Physical Review Letters*, 105(21):214301, 2010.

[108] S. Mora, T. Phou, J. Fromental, and Y. Pomeau. Gravity driven instability in elastic solid layers. *Physical Review Letters*, 113(17):178301, 2014.

[109] L.G. Moretto, K. Tso, N. Colonna, and G.J. Wozniak. New rayleigh-taylor-like surface instability and nuclear multifragmentation. *Physical Review Letters*, 69(13):1884, 1992.

[110] H. W. Müller and W. Zimmermann. Faraday instability in a linear viscoelastic fluid. *Europhysics Letters*, 45:169–174, 1999.

[111] H.W. Müller. Parametrically driven surface waves on viscous ferrofluids. *Physical Review E*, 58(5):6199, 1998.

[112] H.W. Müller, H. Wittmer, C. Wagner, J. Albers, and K. Knorr. Analytic stability theory for faraday waves and the observation of the harmonic surface response. *Physical Review Letters*, 78(12):2357, 1997.

[113] A.I. Murdoch. The propagation of surface waves in bodies with material boundaries. *Journal of the Mechanics and Physics of Solids*, 24(2-3):137–146, 1976.

[114] S.V. Murphy and A. Atala. 3d bioprinting of tissues and organs. *Nature Biotechnology*, 32(8):773, 2014.

[115] S.V. Murphy, A. Skardal, and A. Atala. Evaluation of hydrogels for bio-printing applications. *Journal of Biomedical Materials Research Part A*, 101(1):272–284, 2013.

[116] R. Muthupillai, D.J. Lomas, P.J. Rossman, J.F. Greenleaf, et al. Magnetic resonance elastography by direct visualization of propagating acoustic strain waves. *Science*, 269(5232):1854, 1995.

[117] Y. Ohmasa and M. Yao. Surface waves on non-newtonian viscoelastic liquids. *Physical Review E*, 83(3):031605, 2011.

[118] Y. Onodera and P-K. Choi. Surface-wave modes on soft gels. *The Journal of the Acoustical Society of America*, 104(6):3358–3363, 1998.

[119] D. Paretkar, X. Xu, C. Hui, and A. Jagota. Flattening of a patterned compliant solid by surface stress. *Soft Matter*, 10(23):4084–4090, 2014.

[120] C.B. Park, R.D. Miller, and J. Xia. Multichannel analysis of surface waves. *Geophysics*, 64(3):800–808, 1999.

[121] C.D. Park and T. Nosoko. Three-dimensional wave dynamics on a falling film and associated mass transfer. *AIChE Journal*, 49(11):2715–2727, 2003.

[122] S.J. Park, J.B. Bostwick, V. De Andrade, and J.H. Je. Self-spreading of the wetting ridge during stick-slip on a viscoelastic surface. *Soft Matter*, 13(44):8331–8336, 2017.

[123] N. Perinet, D. Juric, and L.S. Tuckerman. Numerical simulation of faraday waves. *Journal of Fluid Mechanics*, 635:1–26, 2009.

[124] M. Perlin and W.W. Schultz. Capillary effects on surface waves. *Annual Review of Fluid Mechanics*, 32(1):241–274, 2000.

[125] J. Plateau. *Statique expérimentale et théorique des liquides soumis aux seules forces moléculaires*, volume 2. Gauthier-Villars, 1873.

[126] C. Py, P. Reverdy, L. Doppler, J. Bico, B. Roman, and C.N. Baroud. Capillary origami: spontaneous wrapping of a droplet with an elastic sheet. *Physical Review Letters*, 98(15):156103, 2007.

[127] A. Qi, L. Yeo, J. Friend, and J. Ho. The extraction of liquid, protein molecules and yeast cells from paper through surface acoustic wave atomization. *Lab on a Chip*, 10(4):470–476, 2010.

[128] L. Rayleigh. On progressive waves. *Proceedings of the London Mathematical Society*, s1-9(1):21–26, 1877.

[129] L. Rayleigh. On the instability of jets. *Proceedings of the London mathematical society*, 1(1):4–13, 1878.

[130] L. Rayleigh. On waves propagated along the plane surface of an elastic solid. *Proceedings of the London Mathematical Society*, 1(1):4–11, 1885.

[131] B. Roman and J. Bico. Elasto-capillarity: deforming an elastic structure with a liquid droplet. *Journal of Physics: Condensed Matter*, 22(49):493101, 2010.

[132] J. R. Saylor. The role of capillary waves in oceanic air/water gas exchange. *Tellus*, 51B:616–628, 1999.

[133] J. R. Saylor and R. A. Handler. Capillary wave gas exchange in the presence of surfactants. *Experiments in Fluids*, 27:332–338, 1999.

[134] H. Segur, D. Henderson, J. Carter, J.and Hammack, C-M Li, D. Pheiff, and K. Socha. Stabilizing the benjamin-feir instability. *Journal of Fluid Mechanics*, 539:229–272, 2005.

[135] P.N. Shankar. Frequencies of gravity–capillary waves on highly curved interfaces with edge constraints. *Fluid Dynamics Research*, 39(6):457, 2007.

[136] X. Shao, S. A. Fredericks, J. R. Saylor, and J. B. Bostwick. Elastocapillary transition in gel drop oscillations. *Physical Review Letter.*, 123:188002, Oct 2019.

[137] X. Shao, S.A. Fredericks, J.R. Saylor, and J.B. Bostwick. A method for determining surface tension, viscosity, and elasticity of gels via ultrasonic levitation of gel drops. *The Journal of the Acoustical Society of America*, 147(4):2488–2498, 2020.

[138] X. Shao, J. R. Saylor, and J.B. Bostwick. Extracting the surface tension of soft gels from elastocapillary wave behavior. *Soft Matter*, 14(36):7347–7353, 2018.

[139] H.D.C. Smyth and A.J. Hickey. *Controlled Pulmonary Drug Delivery*. Springer, 2011.

[140] P.H. Steen, C. Chang, and J.B. Bostwick. Droplet motions fill a periodic table. *Proceedings of the National Academy of Sciences*, 116(11):4849–4854, 2019.

[141] R.W. Style, R. Boltyanskiy, B. Allen, K.E. Jensen, H.P. Foote, J.S. Wettlaufer, and E.R. Dufresne. Stiffening solids with liquid inclusions. *Nature Physics*, 11(1):82, 2015.

[142] R.W. Style, R. Boltyanskiy, Y. Che, J.S. Wettlaufer, L.A. Wilen, and E.R. Dufresne. Universal deformation of soft substrates near a contact line and the direct measurement of solid surface stresses. *Physical Review Letters*, 110(6):066103, 2013.

[143] R.W. Style, C. Hyland, r Boltyanskiy, J.S. Wettlaufer, and E.R. Dufresne. Surface tension and contact with soft elastic solids. *Nature Communications*, 4(1):1–6, 2013.

[144] R.W. Style, A. Jagota, C. Hui, and E.R. Dufresne. Elastocapillarity: Surface tension and the mechanics of soft solids. *Annual Review of Condensed Matter Physics*, 8:99–118, 2017.

[145] R. Suntornnond, J. An, and C.K. Chua. Bioprinting of thermoresponsive hydrogels for next generation tissue engineering: a review. *Macromolecular Materials and Engineering*, 2016.

[146] S.I. Tamim and J.B. Bostwick. The elastic rayleigh drop. *Soft Matter*, 15(45):9244–9252, 2019.

[147] Y. Tian, R. G. Holt, and R. E. Apfel. Investigation of liquid surface rheology of surfactant solutions by droplet shape oscillations: Theory. *Physics of Fluids.*, 7(12):2938–2949, 1995.

[148] Y. Tian, R. G. Holt, and R.E. Apfel. Investigation of liquid surface rheology of surfactant solutions by droplet shape oscillations: Experiments. *Journal of Colloid and Interface Science.*, 187:1–10, 1997.

[149] M. Tinguely, M.G. Hennessy, A. Pommella, O.K. Matar, and V. Garbin. Surface waves on a soft viscoelastic layer produced by an oscillating microbubble. *Soft Matter*, 12(18):4247–4256, 2016.

[150] C.R. Tipton and T. Mullin. An experimental study of faraday waves formed on the interface between two immiscible liquids. *Physics of Fluids*, 16(7):2336–2341, 2004.

[151] M. Tokita and K. Hikichi. Mechanical studies of sol-gel transition: Universal behavior of elastic modulus. *Physical Review A*, 35(10):4329, 1987.

[152] E. Trinh and T. G. Wang. Large-amplitude free and driven drop-shape oscillations: experimental observations. *Journal of Fluid Mechanics.*, 122:315–338, 1982.

[153] E. Trinh, A. Zwern, and T. G. Wang. An experimental study of small-amplitude drop oscillations in immiscible liquid systems. *Journal of Fluid Mechanics.*, 115:453–474, 1982.

[154] E. H. Trinh. Compact acoustic levitation device for studies in fluid dynamics and material science in the laboratory and microgravity. *Review of Scientific Instruments*, 56(11):2059–2065, 1985.

[155] E. H. Trinh and C. J. Hsu. Equilibrium shapes of acoustically levitated drops. *Journal of Acoustic Society of America.*, 79(5):1335–1338, 1986.

[156] E. H. Trinh, P. L. Marston, and J. L. Robey. Acoustic measurement of the surface tension of levitated drops. *Journal of Colloid and Interface Science.*, 124(1):95–103, 1988.

[157] G.S. Vaiana and R. Rosner. Recent advances in coronal physics. *Annual Review of Astronomy and Astrophysics*, 16(1):393–428, 1978.

[158] G. Vazquez-Una, F. Chenlo-Romero, M. Sanchez-Barral, and V. Perez-Munuzuri. Mass transfer enhancement due to surface wave formation at a horizontal gas–liquid interface. *Chemical Engineering Science*, 55(23):5851–5856, 2000.

[159] C. Wagner, H.W. Müller, and K. Knorr. Faraday waves on a viscoelastic liquid. *Physical Review Letters*, 83(2):308, 1999.

[160] S. Wang, J.M. Lee, and W.Y. Yeong. Smart hydrogels for 3d bioprinting. *International Journal of Bioprinting*, 1(1), 2015.

[161] W. Wang and R. Huang. Wind energy input to the surface waves. *Journal of Physical Oceanography*, 34(5):1276–1280, 2004.

[162] R. C. Weast. *Handbook of Chemistry and Physics*. Chemical Rubber Company, Cleveland, OH, 52 edition, 1972.

[163] M. Westra, D.J. Binks, and W. Van De Water. Patterns of faraday waves. *Journal of Fluid Mechanics*, 496:1–32, 2003.

[164] Q. Xu, K.E. Jensen, R. Boltyanskiy, R. Sarfati, R.W. Style, and E.R. Dufresne. Direct measurement of strain-dependent solid surface stress. *Nature Communications*, 8(1):555, 2017.

[165] Q. Xu, R.W. Style, and E.R. Dufresne. Surface elastic constants of a soft solid. *Soft Matter*, 14(6):916–920, 2018.

[166] L.Y. Yeo, Z. Gagnon, and H.C. Chang. Ac electrospray biomaterials synthesis. *Biomaterials*, 26(31):6122–6128, 2005.

[167] P. Zarrintaj, Z. Manouchehri, S.and Ahmadi, M.R. Saeb, A.M. Urbanska, D.L. Kaplan, and M. Mozafari. Agarose-based biomaterials for tissue engineering. *Carbohydrate Polymers*, 187:66–84, 2018.

[168] X. Zhang and J.F. Greenleaf. Estimation of tissues elasticity with surface wave speed. *The Journal of the Acoustical Society of America*, 122(5):2522–2525, 2007.